Supplementary Information (SI) for Energy & Environmental Science.

Electronic Supplementary Information

Biphasic valorization of byproducts from biodiesel synthesis using floating photochemo-enzymatic domino catalysis

Andrea Rogolino[a] and Erwin Reisner*[a]

[a] Yusuf Hamied Department of Chemistry, University of Cambridge, Cambridge, CB2 1EW UK
* Email: reisner@ch.cam.ac.uk

Supplementary Methods

Additional synthetic procedures

Synthesis of sodium poly(heptazine imide) (Na-PHI): The material was prepared according to a reported procedure.[1, 2] 10 g of melamine was ground with 100 g of NaCl, ball-milled (stainless steel, 25 Hz, 10 min), and annealed in a 500 mL ceramic crucible with a lid under N_2 in a muffle furnace at 600 °C for 4 h (ramp rate 2.3 °C min^{-1}). N_2 was flowed from the top exhaust outlet of the muffle furnace at a flow rate ≈ 1 L min^{-1}. The powder was stirred in boiling water for 1 h, centrifuged (11000 rpm, 10 min), washed with Milli-Q water (3 x 25 mL), and dried overnight at 65 °C.

Synthesis of potassium poly(heptazine imide) (K-PHI): The material was prepared according to a reported procedure.[1] 5.4 g of cyanamide was ground with 54 g of KCl, ball-milled (stainless steel, 25 Hz, 10 min), and annealed in a 500 mL ceramic crucible with a lid under N_2 in a muffle furnace at 600 °C for 4 h (ramp rate 2.3 °C min^{-1}). N_2 was flowed from the top exhaust outlet of the muffle furnace at a flow rate ≈ 1 L min^{-1}. The powder was stirred in boiling water for 1 h, centrifuged (11000 rpm, 10 min), washed with MilliQ water (3 x 25 mL), and dried overnight at 65 °C.

Synthesis of proton poly(heptazine imides) (H-PHI): Protonated cyanamide-functionalised CN_x was prepared according to a reported procedure.[2] 2 mL of 37 wt% aqueous HCl were added to 200 mg of Na-PHI in a 15 mL centrifuge tube. The tube was immediately vortexed and shaken. The sample was centrifuged (11000 rpm, 10 min), the supernatant discarded and washed with Milli-Q water (5 x 40 mL). Finally, the sample was dried overnight at 65 °C.

Synthesis of heptazine/triazine heterojunction carbon nitride (HTCN): the material was prepared according to a reported procedure.[3] Cyanuric acid (1.29 g) and melamine (1.26 g) were dissolved in 20 mL and 40 mL of DMSO, respectively. The melamine solution was added dropwise to the cyanuric acid solution under stirring and stirred for 1 h. The white precipitate was centrifuged (11000 rpm, 10 min), washed with absolute ethanol (3 x 25 mL), and dried overnight at 65 °C. The white solid was annealed at 500 °C for 4 h (ramp rate 2 °C min^{-1}) under Ar (80 mL min^{-1}) in a tube furnace, covering the ceramic boat with a lid. The obtained white solid was mixed and ground with KCl and LiCl in 1:3.3:2.7 wt. ratio in a glove box. The resulting powder was annealed at 600 °C for 4 h (ramp rate 4 °C min^{-1}) under Ar in a tube furnace. The obtained sample was stirred for 1 h in boiling water, centrifuged (11000 rpm, 10 min), washed with Milli-Q (3 x 25 mL), and dried overnight at 65 °C.

Synthesis of joint carbon nitride with multiple order-disorder interfaces (CN-NH_4-NaK): The material was prepared according to a reported procedure.[4] 10 g of CN_x were ground with 10 g of NH_4Cl and annealed at 550 °C for 4h (ramp rate 5 °C min^{-1}) in a crucible with a lid under air. The obtained powder was washed with

Milli-Q water followed by centrifugation (3 x 25 mL, 11000 rpm, 10 min) and dried overnight at 65 °C. Then, all the obtained powder was ground with 3.36 g of NaCl and 2.64 g of KCl and annealed in a crucible with a lid at 550 °C for 4 h (ramp rate 2.3 °C min^{-1}) under air. The sample was stirred in boiling water for 1 h, centrifuged (11000 rpm, 10 min), washed with Milli-Q water (3 x 25 mL), and dried overnight at 65 °C.

Synthesis of chloride-iodide poly(heptazine imide) (CN-KCl/KI): The material was prepared according to a reported procedure.[5] 10 g of melamine were ground with 0.745 g of KCl and 1.66 g of KI, annealed in a crucible with a lid at 550 °C for 4 h (ramp rate 2 °C min^{-1}). The obtained powder was washed with Milli-Q water followed by centrifugation (3 x 25 mL, 11000 rpm, 10 min) and dried at 65 °C overnight.

Additional catalytic tests

Screening of simulated solar light intensities for photocatalytic H_2O_2 production: 2 mL of 30 wt% aqueous glycerol, 2 mL of 40 wt% oleic acid in ethyl acetate, and 50 mg of H-CN$_x$/PP were added to a custom glass reactor for top-down irradiation (diameter: 3 cm, total volume: 50 mL, **Figure 1**). The reactor was sealed with a screwcap and a rubber septum, purged with O_2 for 5 minutes, and irradiated with a LOT-QD LS0816-H large area solar simulator with an Air Mass 1.5 Global (AM 1.5G, 100 mW cm^{-2}, 1 sun) solar filter for 2 h with no stirring or shaking. A 400 nm cutoff filter was placed at the top of the photoreactor to prevent UV-driven H_2O_2 decomposition. Intensities higher than 1 sun (>100 mW cm^{-2}) were achieved by solar concentration with a commercial Fresnel lens (XL Full Page, 3x magnification, PVC). A front surface SiO_2-protected 8” square aluminum mirror (Thorlabs) was used to deflect light from the solar simulator to the top of the photoreactor. The light intensity was measured with a Newport 843-R optical power meter, adjusting the distance between the lens and the photoreactor.

Screening of cis-cyclooctene epoxidation in domino photochemo-enzymatic epoxidation: To assess the effect of alkene concentration in the organic phase on epoxidation yield, 2 mL of 30 wt% glycerol, 2 mL of cis-cyclooctene in ethyl acetate at different vol.%, 20 mg of H-CN$_x$/PP, and 40 mg iCALB were added to a glass vial (diameter: 2 cm, total volume 11.5 mL). The vial was sealed with a crimp-cap and a rubber septum, and the mixture was purged with O_2 for 2 min. The vial was irradiated (LED, 450 nm, 40±4 mW cm^{-2}) at 25 °C for 16 h under 250 rpm shaking.

Tests to assess the iCALB-catalyzed cis-cyclooctene conversion to cyclooctene oxide as a function of aqueous H_2O_2 concentration were run in the dark and in the absence of photocatalyst, with 100 mM cis-cyclooctene in ethyl acetate as the organic phase, at 40 °C for 16 h.

In another set of tests, the highest conversion of cis-cyclooctene achievable with *in-situ* photogenerated H_2O_2 was assessed with 30 wt% aqueous glycerol, 100 mM cis-cyclooctene in ethyl acetate, 20 mg H-CN$_x$/PP, 40 mg iCALB, 1 atm O_2, blue LED (450 nm, 40±4 mW cm^{-2}) irradiation at 25 °C for 24h.

Discontinuous operation of photochemo-enzymatic domino: Discontinuous tests were run periodically replacing the aqueous phase of the biphasic system, either externally added aqueous H_2O_2 or 30 wt% aqueous glycerol for *in-situ* production of H_2O_2. 3 mL of aqueous phase, 3 mL of 40 wt% oleic acid in ethyl acetate, 50 mg of H-CN$_x$/PP, and 40 mg of iCALB were added to a custom glass reactor for top-down irradiation (diameter: 3 cm, total volume 50 mL, **Figure 1**). The reactor was sealed with a screwcap and a rubber septum, purged with O_2 for 5 minutes, and irradiated with a G2V Sunbrick LED Solar Simulator (AM 1.5G, 100 mW cm^{-2}, 1 sun) under 100 rpm shaking. Every 5 h, the organic and aqueous phases were sampled, and the aqueous phase was replaced with a fresh solution.

Conditions for additional catalytic tests and controls are reported in the caption of relevant tables and figures.

Investigation of iCALB deactivation

To test the effect of aqueous H_2O_2 concentration on iCALB deactivation, 2 mL of aqueous H_2O_2 at different concentrations (10 mM, 100 mM, 1000 mM), 2 mL 40 wt% oleic acid, and 40 mg iCALB were added to a glass vial (diameter: 2 cm, total volume 11.5 mL). The vial was shaken at 250 rpm in the dark at 37 °C for 24 h. To assess the kinetics of iCALB deactivation, the test was repeated with 10 mM aqueous H_2O_2 and the vial was shaken for different times within 8 h. After the incubation time, the mixture was filtered, washed with ethyl acetate, and the collected iCALB was left to dry at room temperature and stored overnight at 4 °C. 10 mg of collected iCALB were added to 1 mL of 100 mM lauric acid in 1-propanol. The vial was shaken at 250 rpm in the dark for 30 min. The activity of the lipase was assessed from the quantification of synthesized propyl laurate (PL), and reported as propyl laurate units (PLU), defined as $\mu mol_{\text{propyl laurate}}\ min^{-1}\ g^{-1}_{\text{iCALB}}$.

Determination of the CN_x content by TGA

The content of CN_x in the floating composites was determined from the second major weight loss detected in the TGA trace, corrected by the amount of adsorbed water on CN_x lost by evaporation below 300 °C, corresponding to 23% weight of CN_x.[6]

Determination of the optical band gap of materials from Tauc plots

Optical band gaps were determined from the elaboration of the diffuse reflectance UV-Vis spectra into Tauc plots under the assumptions of the Kubelka-Munk theory.[7] Briefly, the Tauc equation implies a correlation between the linear absorption coefficient *α* and the energy band gap *Eg*:

$$\alpha h\nu = C(h\nu - Eg)^n$$

Where *h* is the Planck constant ($6.626 \cdot 10^{-34}$ J s), *v* is the radiation frequency and *C* is a constant. *n* may assume different values depending on the nature of the band gap. For a direct, allowed transition, *n* is equal to ½. If the material scatters light diffusively, the signal acquired from diffuse reflectance spectroscopy is proportional to the absorption coefficient. Hence, under these conditions the Tauc equation becomes:

$$(\alpha h\nu)^2 = C'(h\nu - Eg)$$

If the first term is plotted against hv, the intersection between the tangent to the point of highest slope and the horizontal axis determines Eg.

Determination of the valence band edge position from ultraviolet emission spectroscopy

Valence band edge positions were determined from UPS analysis using a He I source ($h\nu$ = 21.2 eV). Binding energies were referenced to the Fermi level (E_F) of the material. Spectra were elaborated according to the theory and interpretation relevant to semiconductor materials.[8, 9]

The secondary electron cutoff energy (E_{cutoff}) was determined from the onset at high binding energies (**Figure S3**). E_{cutoff} is defined as the difference between the energy of the source and the work function of the material (Φ):

$$E_{cutoff} = h\nu - \Phi = h\nu - E_F \quad \Leftrightarrow \quad E_F = h\nu - E_{cutoff}$$

The energy difference between the valence band edge and the Fermi level (E_{VB} - E_F) is determined from the onset at lower binding energies (**Figure S3**). The energy of the valence band edge referenced to the vacuum is calculated as:

$$E_{VB} = h\nu - E_{cutoff} + (E_{VB} - E_F)$$

Both E_{VB} and E_F determined from UPS analysis are referenced to vacuum. Energies can be converted to the standard hydrogen electrode (SHE) potential through the conversion formula:[10]

$$E(V\ vs\ SHE) = E(eV\ vs\ vacuum) - 4.44\ eV$$

Determination of external quantum efficiency (EQE)

The EQE was determined by irradiating the floating H-CN$_x$/PP (10 mg) and iCALB (20 mg) in a mixture of 30 wt% aqueous glycerol (1 mL) and 40 wt% oleic acid in ethyl acetate (1 mL) in a 3 mL vial that was purged with O_2 for 5 min. A LOT-QD LS0816-H solar simulator was used as the irradiation source and the light was filtered with a LOT-QD MSH-300 monochromator. Light was deflected to the top of the vial with a front surface SiO_2-protected 8” square aluminum mirror (Thorlabs). The incident power at the height of liquid-liquid interface was measured with a Thorlabs PM130D power meter. After 4 h of irradiation, epoxides in the organic phase was quantified. The EQE was calculated with the following formula, assuming H_2O_2 production as a two-electron reduction process, and a 1:1 stoichiometry between H_2O_2 and epoxides:

$$EQE(\%) = \frac{n_{epoxide} \cdot 2}{n_{photons}} \cdot 100 = \frac{mol_{epoxide} \cdot 2 \cdot N_A \cdot h \cdot c}{P \cdot t \cdot \lambda} \cdot 100$$

Where $n_{epoxide}$ is the number of molecules of epoxide produced, $n_{photons}$ is the total number of incident photons, $mol_{epoxide}$ are the moles of epoxide produced, N_A is the Avogadro’s number ($6.022 \cdot 10^{23}$ mol^{-1}), h is the Planck constant ($6.626 \cdot 10^{-34}$ J s), c is the speed of light ($2.9979 \cdot 10^{8}$ m s^{-1}), P is the power of the incident light, t is the irradiation time, and λ is the irradiation wavelength.

Treatment of data

Given errors of analytical measurements were calculated as the unweighted mean standard deviation (σ) of triplicates, unless otherwise stated. σ was calculated as:

$$\sigma = \sqrt{\frac{\sum_i (x_i - \bar{x})^2}{n - 1}}$$

Where n is the number of repeated measurements, x_i is the value of a single measurement i, and $\bar{x}$ is the unweighted mean.

Supplementary Note 1: Investigation of the enhanced photocatalytic H_2O_2 evolution with protonated poly(heptazine imides) (H-CN_x)

To understand the role of CN_x protonation on the improved photocatalytic H_2O_2 production rate, we conducted further investigations to compare the physical and electronic properties of H-CN_x and the unprotonated precursor K-CN_x.

Upon protonation, K-CN_x underwent significant modifications of its optical properties, as evidenced by the bleaching of the material, turning from yellow to white (**Figure S2e**). Correspondingly, the optical bandgap increased from 2.65 eV in K-CN_x to 2.87 eV in H-CN_x, as determined by diffuse reflectance UV-Vis spectroscopy (**Figure S2e**, Table S1). CN_x bleaching in acidic environments is a well-reported phenomenon.[2, 11] The increased bandgap of H-CN_x results in the utilization of a narrow region of the solar spectrum, including only a portion of violet light and the UV. Therefore, the enhanced activity of H-CN_x cannot be attributed to enhancements in light absorption. The valence band (VB) edge position was determined by ultraviolet photoemission spectroscopy (UPS) (**Figure S3a**). Conduction band (CB) edge positions were determined by subtracting the energy of the bandgap from the energy of the VB maximum. Both catalysts showed similar oxidative potential, with VB maxima of 2.54 V and 2.47 V vs SHE for K-CN_x and H-CN_x, respectively (**Figure S2f**, Table S1). Protonation resulted in a shift of the CB maximum to more negative potentials for H-CN_x (–0.38 V vs SHE) compared to K-CN_x (–0.11 V vs SHE). Nevertheless, both potentials are well above the standard reduction potential of O_2 to H_2O_2 (0.68 V vs SHE).[12] Edge cyanamide (-N=C=N$^-$) units, which have been proposed as key functional groups in the polymeric structure of CN_x for the suppression of charge recombination,[13] were present in both K-CN_x and H-CN_x, as evidenced by the typical stretching frequency at 2181 cm^{-1} in their infrared (IR) spectra (**Figure S2g**). In conclusion, the reason for H-CN_x enhanced photocatalytic performance is likely not rooted in the photophysics of the material.

We then assessed whether differences in the physical properties of H-CN_x and K-CN_x could play a role in photocatalytic activity. Due to the protonation of the cyanamide units into -N=C=NH (**Figure S2d**, H-CN_x is expected to undergo a loss of hydrophilicity compared to the ionic K-CN_x. The higher hydrophobicity of H-CN_x might indeed explain its higher loading of 37.1 % in the CN_x/PP floatable composite, compared with 25.3 % obtained from K-CN_x, as determined by thermogravimetric analysis (TGA) (**Figure S2h**, Table S2). Likewise, H-CN_x/PP fabrication resulted in a floating fraction of 37.3±3.2 %, while K-CN_x/PP yielded only 26.7±4.3 % of floatable material (Table S2). The better incorporation of H-CN_x with plastic might result from a lower tendency of H-CN_x to leach out into water in the process of separation of the floating fraction. The higher photocatalyst content in the composite also partly explains the superior photocatalytic activity of H-CN_x/PP compared to K-CN_x/PP, although it is not sufficient to rationalize the difference observed when powder dispersions were used at the same concentration. To probe whether the different hydrophilicity of the materials plays a relevant role in their dispersion ability or affinity to aqueous solutions, we performed contact angle measurements. Both H-CN_x and K-CN_x showed very high hydrophilicity, with contact angles of 4.6° and 4.8°, respectively (**Figure S4**). The observation implies that H-CN_x undergoes fast deprotonation in water, restoring the anionic -N=C=N$^-$ responsible for water affinity. Measurements of ζ-potential of aqueous dispersions supported this hypothesis, reporting very close potentials of –34.7±0.3 and –31.2±0.3 mV for H-CN_x and K-CN_x, respectively (Table S3).

The fast deprotonation of H-CN_x in neutral water suggests that the catalytic enhancement might simply originate from *in-situ* acidification of the reaction medium. Indeed, the pH of 2 mg mL^{-1} aqueous dispersions of H-CN_x and K-CN_x in Milli-Q water was 4.2 and 8.2, respectively (Table S3). H_2O_2 is generally stored in mildly acidic conditions (pH 3-5) to prevent its faster decomposition at neutral to alkaline environments.[14-16] Indeed, when 2 mg of material was dispersed in 2 mL of 10 mM aqueous H_2O_2 solution and irradiated at 450 nm (40±4 mW cm^{-2}) under inert atmosphere (1 atm N_2) at 25 °C, 48.8±0.03 % of H_2O_2 was consumed in 2 h in the presence of K-CN_x, while the value dropped to 23.4±0.10 % with H-CN_x under the same conditions (**Figure S5b**). Finally, when the pH of a K-CN_x solution was adjusted to ~4 by the addition of 0.1 M HCl, the catalyst performed as H-CN_x with no further additives in the photocatalytic ORR to H_2O_2 coupled with glycerol oxidation (Table S4).

Collectively, the results lead to conclude that the superior photocatalytic activity of H-CN_x in the photocatalytic O_2-to-H_2O_2conversion can be only attributed to the *in-situ* acidification of the reaction medium to pH 4-5, suppressing H_2O_2 decomposition.

Supplementary Note 2: Non-innocent role of ethyl acetate in iCALB-catalyzed epoxidation

The superior performance of ethyl acetate as a solvent in iCALB-catalyzed epoxidation was explained by its participation to the chemical reaction. Ethyl acetate undergoes enzyme-catalyzed hydrolysis to acetic acid and ethanol, followed by enzymatic perhydrolysis to generate peracetic acid which participates as an epoxidizing agent (**Figure S9**). Interestingly, the role of ethyl acetate was also observed in preliminary tests on cis-cyclooctene epoxidation, where the yield of cyclooctene oxide suddenly dropped from 48.9±1.8 mmol L^{-1} to 9.9±0.1 mmol L^{-1} moving from 90 vol.% substrate in ethyl acetate to neat cis-cyclooctene (**Figure S7c**). In the absence of glycerol in the aqueous solution, H_2O_2 was indeed generated by ORR coupled with the oxidation of ethanol of acetaldehyde in stoichiometric amounts (**Figure S10**, Table S6). Nevertheless, in the presence of excess glycerol (30 wt% or higher), acetaldehyde production was negligible, indicating that glycerol participated as the main electron donor (Table S6). Moreover, ethyl acetate is an excellent choice of organic solvent for its low toxicity and environmental impact, improving the sustainability of the whole process.[17]

Supplementary Note 3: Discontinuous vs batch operation of the solar-driven photochemo-enzymatic domino

The epoxidation yield of oleic acid under simulated solar light reached a plateau when the reaction was extended to 20 h (2.9±0.1 μmol cm^{-2}, 6.8±0.2 mmol L^{-1}, **Figure S23a**). When the domino reaction was run replacing the 30 wt% aqueous glycerol solution every 5 h, the epoxidation proceeded with a linear increase up to 4.6±0.3 μmol cm^{-2} (10.8±0.7 mmol L^{-1}) of product in the organic phase, corresponding to a 1.6-fold increase compared to the batch operation (**Figure S23b**). Given the inherent limitations imposed by mass transfer in the phase-segregated assembly, we hypothesized that the halt of the epoxidation reaction could be attributed to a combination of O_2 consumption at the interface and H_2O_2 diffusion into the bulk of the aqueous phase, thus preventing its *in-situ* utilization in the domino. Experimental results reported in **Figure S6** and finite element simulations discussed in Supplementary Notes 4 and 5 give credit to this hypothesis.

As opposed to our previous work,[6] where the main goal of the macroscopic liquid|solid|liquid separation was the compartmentalization of products, the design of a domino reaction requires to maximize the conversion of an *in-situ* generated intermediate at the liquid-liquid interface, before its dilution in the bulk. Therefore, we envisioned that a periodic extraction and replacement of the aqueous phase should reset a high interfacial concentration of H_2O_2, that would instead stagnate in the lower layers of the bottom phase after prolonged operation in batch.

To simulate the steady state in H_2O_2 concentration obtained from the trade-off between H_2O_2.generation and consumption (**Figure S14a**),[6] we compared the epoxide generation over 20 h in the presence of exogenous aqueous H_2O_2 (~10 mM) in batch and discontinuous operation, where the latter consisted of replacing the aqueous H_2O_2 every 5 h. As expected, the epoxidized oleic acid reached a high of only 3.3 mmol L^{-1} (1.4 μmol cm^{-2}) in 20 h when H_2O_2 was only added once and let react. The H_2O_2 concentration plummeted from 9.1 mmol L^{-1} to 0.4 mmol L^{-1} in just 10 h, and was totally consumed after 20 h (**Figure S23c**).

When the aqueous H_2O_2 phase was replaced every 5 h, the epoxide in the organic phase raised steadily up to 14.1±0.1 μmol cm^{-2} (33.1±0.3 mmol L^{-1}) (**Figure S23d**). The cumulative H_2O_2 consumption was 15.5±0.4 mmol L^{-1}, indicating a higher utilization of the peroxide. The periodic replacement of aqueous glycerol in the domino scenario allows to re-initiate the interfacial H_2O_2 generation – i.e. to restore a high concentration of H_2O_2 at the interface, as simulated with exogenous H_2O_2 – averting the stagnant steady state condition.

The beneficial effect of the discontinuous strategy also suggests that the interrupted epoxidation is likely not attributed to enzyme deactivation, as evidence by the good recyclability of the whole system (**Figure 2d**) Indeed, under the typical conditions for the solar-driven domino defined above, when fresh iCALB was added after 20 h of reaction, no difference in epoxide production in the following 5 h was observed (**Figure S23e**).

Supplementary Note 4: Kinetic models for finite element simulations studies

H_2O_2 evolution was modelled as a system of equations including H_2O_2 synthesis from oxygen reduction coupled with glycerol (Gly) oxidation to glyceraldehyde (GAl) (1), H_2O_2 photocatalytic depletion by disproportionation (2), and H_2O_2 perhydrolysis by iCALB to convert oleic acid (OA) to peroxy oleic acid (POA) (3):[18, 19]

$$\mathrm{O_2{+}Gly} \xrightarrow{k'_1} \mathrm{H_2O_2{+}GAl} \tag{1}$$

$$\mathrm{H_2O_2} \xrightarrow{k_2} \tfrac{1}{2}\mathrm{O_2{+}H_2O} \tag{2}$$

$$\mathrm{H_2O_2{+}OA} \xrightarrow[iCALB]{k'_3} \mathrm{POA{+}H_2O} \tag{3}$$

The rate of hydrogen peroxide generation is given by the following linear differential equation:

$$\frac{d[\mathrm{H_2O_2}]}{dt} = k_1[\mathrm{O_2}] - (k_2 + k_3)[\mathrm{H_2O_2}] \tag{4}$$

Where k_1 and k_3 are pseudo first-order kinetic coefficients related to k'_1 and k'_3 assuming a constant concentration of glycerol and oleic acid, that are added in large excess in the aqueous and organic phase, respectively:

$$k_1 = k'_1[\mathrm{Gly}] \tag{5}$$

$$k_3 = k'_3[\mathrm{OA}] \tag{6}$$

H_2O_2 perhydrolysis by iCALB was assumed to follow a Michaelis-Menten kinetics. k_3 was taken as the ratio between the maximum rate (V_{max}) and the Michaelis constant (K_M), assuming that the H_2O_2 concentration at the interface was maintained low due to rapid *in-situ* generation and consumption, so to fall within the linear regime of the Michaelis-Menten kinetics.

Accordingly, O_2 reaction rate was modelled as:

$$\frac{d[\mathrm{O_2}]}{dt} = -k_1[\mathrm{O_2}] \tag{7}$$

Glyceraldehyde production was assumed to proceed at the same rate of oxygen consumption:

$$\frac{d[\mathrm{GAl}]}{dt} = k_1[\mathrm{O_2}] \tag{8}$$

The synthesis of epoxy oleic acid (EOA) was modelled as a domino process consisting of H_2O_2 perhydrolysis by iCALB to generate peroxy fatty acids, followed by irreversible Prilezhaev epoxidation:

$$\mathrm{H_2O_2{+}OA} \xrightarrow[iCALB]{k_3'} \mathrm{POA + H_2O} \tag{9}$$

$$\mathrm{POA + OA} \xrightarrow{k_4} \mathrm{EOA} \tag{10}$$

Peroxy fatty acids were assumed to be labile intermediates, so that a steady-state approximation could be applied:

$$\frac{d[\mathrm{POA}]}{dt} = k_3'[\mathrm{H_2O_2}][\mathrm{OA}] - k_4[\mathrm{POA}][\mathrm{OA}] = 0 \tag{11}$$

$$[\mathrm{POA}] = \frac{k_3'}{k_4}[\mathrm{H_2O_2}] \tag{12}$$

$$\frac{d[\mathrm{EOA}]}{dt} = k_4[\mathrm{POA}][\mathrm{OA}] = k_3'[\mathrm{H_2O_2}][\mathrm{OA}] = k_3[\mathrm{H_2O_2}] \tag{13}$$

All chemical reactions were assumed to occur at the interface between the liquid phases, while no reaction was modelled in the bulk. Kinetic coefficients are reported in Table S11. k_1 and k_2 were experimentally determined in our previous work.[6] k_3 was approximated as the ratio between V_{max} and K_M determined for β-pinene epoxidation with iCALB.[20]

Supplementary Note 5: Finite element modeling

Discontinuous operation.

The study aimed to investigate the effect of discontinuous (periodical) replacement of the aqueous phase on the average H_2O_2 concentration at the interface, and the resulting epoxide generation in the organic phase.

The simulation employed a 3D axisymmetric model consisting of a cylindrical reactor with a diameter of 3 cm and a height of 2 cm. The interface was modelled as a cylindrical region at half the height of the reactor having a thickness of 1 mm and partitioned in two halves assigned to ethyl acetate (upper) and water (lower).

The simulation was run using the *transport of diluted species* physics. The governing equations incorporated in the model included mass transport equations to account for diffusive transport of hydrogen peroxide, oxygen, and epoxide:

$$\text{i. } \frac{\partial c_i}{\partial t} + \nabla \cdot \boldsymbol{J}_i = R_i$$

$$\text{ii. } \boldsymbol{J}_i = -D_i \nabla c_i$$

where the dependent variables include velocity, and concentration (c_i). D_i is the diffusion coefficient, $\boldsymbol{J}_i$ is the flux and R_i is the reaction rate expressed for each species as detailed in Supplementary Note 4, and summarized by the equations below:

$$\frac{d[H_2O_2]}{dt} = k_1[O_2] - \ (k_2 + k_3)[H_2O_2]$$

$$\frac{d[O_2]}{dt} = -k_1[O_2]$$

$$\frac{d[Epoxide]}{dt} = k_3[H_2O_2]$$

Reaction terms were included only in the interfacial region. Relevant kinetic parameters are reported in Table S11. Partition and diffusion coefficients in water and ethyl acetate for each species are reported in Table S12. Initial values were set to 8.91 mmol L^{-1} and 1.22 mmol L^{-1} for O_2 in ethyl acetate and water, respectively,[21] and 0 mmol L^{-1} for H_2O_2 and epoxide. Time dependent studies to simulate the concentration profiles of all species were run to span a reaction time of 20 h, with a time step of 0.2 h. Discontinuous operation was simulated by resetting O_2 and H_2O_2 in the aqueous phase to 1.22 mmol L^{-1} and 0 mmol L^{-1}, respectively, every 5 h. For comparison, batch (static) operation was simulated omitting the reset event.

Simulations resulted in a higher average concentration of H_2O_2 at the interface under discontinuous compared to static operation (**Figures S24, S25a**, Supplementary Videos 1-2). With no replacement of the aqueous phase, H_2O_2 slowly diffused to the bulk of the aqueous phase, where it could not undergo perhydrolysis by iCALB. Conversely, periodically replacing the aqueous phase maintained a higher amount of H_2O_2 in the reacting region throughout the reaction time. The result is attributed to the replenishment of O_2, whose rapid photocatalytic conversion to H_2O_2 at the interface outcompetes the drawback of resetting the peroxide concentration to 0 mmol L^{-1} in the whole aqueous phase. While epoxide concentration in the organic phase approaches a plateau under static operation, it keeps increasing in discontinuous mode (**Figure S25c**). As the effect is essentially a consequence of O_2 replenishment, simulations predict an even higher epoxide generation rate with replacement of both phases, or by simple periodical O_2 purging (**Figure S25b,d**).

Continuous operation

The study simulated the evolution of concentration profiles of hydrogen peroxide, oxygen, epoxide, and glyceraldehyde in a box reactor under flow operation. The purpose of the simulation was to compare the spatial evolution of each chemical species and the yield of extraction of epoxide from the organic phase and glyceraldehyde from the aqueous phase under different flow modes (dual flow co-current, dual flow counter-current, mono aqueous flow, mono organic flow). In addition, the yield of product extraction under the optimal flow mode and at different flow rates was investigated.

The box reactor was modelled as a 2D surface of 10 cm width and 1 cm height. The interface was modelled as a cylindrical region at half the height of the reactor having a thickness of 1 mm and partitioned in two halves assigned to ethyl acetate (upper) and water (lower).

The simulation was run using a Multiphysics model including the *transport of diluted species* and the *laminar flow* physics. The governing equations incorporated in the model included the Navier-Stokes and continuity equations to describe fluid flow, and mass transport equations to account for diffusive and convective transport of hydrogen peroxide, oxygen, epoxide, and glyceraldehyde:

$$\text{i. } \frac{\partial c_i}{\partial t} + \nabla \cdot \boldsymbol{J}_i + \boldsymbol{u} \cdot \nabla c_i = R_i$$

$$\text{ii. } \boldsymbol{J}_i = -D_i \nabla c_i$$

$$\text{iii. } \rho \frac{\partial \boldsymbol{u}}{\partial t} + \rho(\boldsymbol{u} \cdot \nabla)\boldsymbol{u} = \nabla \cdot [-p\mathbf{I} + \mathbf{K}] + \mathbf{F}$$

$$\text{iv. } \rho \nabla \cdot \boldsymbol{u} = 0$$

where the dependent variables include velocity ($\boldsymbol{u}$), pressure (p), and concentration (c_i). ρ is the fluid density, $p\mathbf{I}$ is a pressure term where p is pressure in the fluid coupled with the identity tensor **I** for isotropic distribution. **K** is a viscous stress tensor to account for viscosity-driven friction, **F** is the tensor of external forces acting on the fluid. D_i is the diffusion coefficient, $\boldsymbol{J}_i$ is the flux and R_i is the reaction rate expressed for each species as detailed in Supplementary Note 4, and summarized by the equations below:

$$\frac{d[H_2O_2]}{dt} = k_1[O_2] - (k_2 + k_3)[H_2O_2]$$

$$\frac{d[O_2]}{dt} = -k_1[O_2]$$

$$\frac{d[Epoxide]}{dt} = k_3[H_2O_2]$$

$$\frac{d[Glyceraldehyde]}{dt} = k_1[O_2]$$

The diffusion coefficient of hydrogen peroxide was estimated to be $1.6 \cdot 10^{-9}$ m^2 s^{-1} in water and 10^{-8} m^2 s^{-1} in ethyl acetate to approximate its behavior in the aqueous phase.[22, 23]

Reaction terms were included only in the interfacial region. Relevant kinetic parameters are reported in Table S11. Partition and diffusion coefficients in water and ethyl acetate for each species are reported in Table S12. Initial concentration values were set to 8.91 mmol L^{-1} and 1.22 mmol L^{-1} for O_2 in ethyl acetate and water, respectively,[21] and 0 mmol L^{-1} for H_2O_2, epoxide, and glyceraldehyde. Simulations were run under the following flow modes:

- Dual flow co-current: incoming horizontal aqueous and organic flow of same direction;
- Dual flow counter-current: incoming horizontal aqueous and organic flow of opposite directions;
- Mono aqueous flow: incoming horizontal aqueous flow, organic phase constrained between walls;

- Mono organic flow: incoming horizontal organic flow, aqueous phase constrained between walls.

The entire side boundaries of each phase were selected as the inlets and outlets of flows, where relevant. Since the incoming fluids are fresh, oxygen-saturated, aqueous glycerol and oleic acid in ethyl acetate, the concentrations of H_2O_2, O_2, epoxide, and glyceraldehyde were set to 0 mmol L^{-1} at each inlet, while the concentration of O_2 was set to 1.22 mmol L^{-1} and 8.91 mmol L^{-1} at the aqueous and organic inlets, respectively. Flow rates were set to 1 mL min^{-1} for all non-zero flows for each simulation. Time dependent studies to simulate the concentration profiles of all species were run to span a reaction time of 60 min, with a time step of 1 min. average concentration of products at the outlets were calculated as line averages over the relevant boundaries.

Simulated concentration profiles for each species shows that the choice of flow mode highly affects the distribution of products at the outlets of the reactor (**Figure 4e**, **Figures S27-30**). Dual flow counter-current operation resulted in the highest epoxide concentration at the outlet of the upper phase, with a seemingly linear increase up 19.8 mmol L^{-1} to after 60 min. Indeed, counter-current operation ensures optimal O_2 supply, in a way that keeps O_2 concentration at the interface high throughout the length of the reactor. Opposite flows also generate a stagnant region at the interface, leading to a higher H_2O_2 residence time. In co-current mode, both O_2 inlets located on the same side of the reactor results in a gradual consumption of O_2 across the x axis and an accumulation of H_2O_2 that cannot react sufficiently fast before it is conveyed out by co-directional flows.

For glyceraldehyde production, dual flows yielded significantly lower amount of product at the aqueous outlet than mono flows. The outcome is likely attributed to the low aqueous diffusion coefficient of glyceraldehyde (0.25 10^{-9} m^2 s^{-1}),[24] that results in product mass transfer majorly driven by convection and a high dilution at the outlet port before it can diffuse to the bulk of the aqueous phase. In counter-current mode, simulations clearly illustrate the formation of a stagnant region of glyceraldehyde where the product is confined, because of slow transfer from the interface to the bulk (**Figure 4**). Conversely, mono flows ensure sufficient O_2 availability in the given reaction time and concentration of the product in the aqueous phase. In particular, when the aqueous phase is physically constrained, O_2 is replenished continuously in the organic phase, where it benefits from higher solubility (8.91 mmol L^{-1}) and diffusion coefficient (3.46 10^{-9} m^2 s^{-1}), while glyceraldehyde can accumulate in the aqueous phase, resulting in the highest number of moles extracted after 60 min (17.1 mmol). Constraining the organic phase also limits glyceraldehyde losses from convection by halving the overall flow rate at the interface, resulting in a continuous increase of product concentration at the outlet and a total number of extracted moles of 15.2 mmol.

We then assessed how flow rates affect the outlet concentration of epoxide and glyceraldehyde (**Figure S30**). Counter-current and co-current modes were chosen for epoxide and glyceraldehyde, respectively. As expected, there is a trade-off between the rate of solution extraction and the dilution of the products in the incoming flow, resulting in a maximum in the amount of product extracted vs flow rate (**Figure S30a**). For the epoxide, 1 mL min^{-1} resulted in the highest outlet epoxide concentration after 60 min (19.7 mmol L^{-1}). At 10 mL min^{-1}, product dilution dominated resulting in a final outlet concentration of 8.9 mmol L^{-1}. At lower flow rates, the reaction was limited by the oxygen supply, so that final outlet concentrations dropped to 11.5 mmol L^{-1} and 8.6 mmol L^{-1} at 0.1 mL min^{-1} and 0.05 mL min^{-1}, respectively.

A similar trade-off was observed for glyceraldehyde in the aqueous phase under co-current flow mode, although product dilution played a major role, which is again due to the low diffusion coefficient of glyceraldehyde (**Figure S30b**). At 1 mL min^{-1}, the outlet concentration plateaued at 4.05 mmol L^{-1}, likely due to the formation of a stagnant region. 0.1 mL min^{-1} and 0.05 mL min^{-1} both yielded an outlet concentration of 8.4 mmol L^{-1}, while at 10 mL min^{-1}, the dilution extent was so high that the outlet aqueous solution had a constant low glyceraldehyde concentration of 1.4 mmol L^{-1}.

We would like to stress that, although we appreciate that numerical results of all simulations are in the same order of magnitude of experimental data and occasionally in good agreement (e.g. average epoxide concentration in ethyl acetate in a batch cylindrical reactor: simulated 6.49 mmol L^{-1} vs experimental 3.8±0.33 mmol L^{-1} from used vegetable oil after 4 h reaction, with a relative error of 70%), finite element modeling studies were run majorly for comparative purposes, to determine the relative accumulation or depletion of species in static vs discontinuous operation, and under different flow modes and rates in continuous operation. Experimental validation of simulated numerical results is beyond the scope of this research.

Supplementary Note 6: Comparative life cycle assessment and simplified techno-economic analysis

A comparative life cycle impact assessment (LCIA) was performed to evaluate the environmental impact of decentralized fatty waste valorization consisting of separate processes for biodiesel synthesis, epoxidation of unsaturated fatty waste, and glyceraldehyde synthesis from glycerol, and integrated fatty waste valorization for combined biodiesel synthesis and conversion of the by-products unreacted fatty acids and glycerol into epoxides and glyceraldehyde, respectively, in the same plant. All processes were analyzed for a cradle-to-gate assessment. Product purification and transportation were not included.

The LCIA for the integrated photocatalytic domino valorization of fatty waste was initially evaluated for the base production of 100 g of epoxidized fatty acid. By extrapolation from the experimental results of this work – based on the results of 48 h solar irradiation of the large scale reactor – the same process also yields 152 g of glyceraldehyde and 6.29 kg of biodiesel. The decentralized method was modelled as three separate processes for the synthesis of the same amounts of epoxidized fatty acids, glyceraldehyde, and biodiesel.

Process diagrams are illustrated in **Figure S32**. Complete inventories including all outputs, inputs, and emissions are reported in Tables S13-16. The domino process was modelled replacing H-CN$_x$ with H-PHI, due to the lower environmental impact of the latter (synthesized from melamine and NaCl),[1] and expected similar utilization of H_2O_2 (**Figure S1**).

The inventory integrated photocatalytic domino valorization of fatty waste was fully based on the experimental procedures and outcomes of this work.

For decentralized production, a plant for tall oil epoxidation was evaluated. Tall oil was chosen as a more convenient fatty acids-rich by-product than used vegetable oils by-products.[25] Indeed, tall oil yield is between 30 and 50 kg per tonne of produced kraft pulp, and its production is projected to increase above 2.2 million tonnes in 2030.[26, 27] Unsaturated fatty acids are generally obtained in lower yields from biodiesel synthesis (Table 1), and are rather fully converted into fatty acids methyl esters (FAME) or soap. The evaluated protocol for tall oil epoxidation was based on patented technologies.[28, 29] The process consisted of acid-catalyzed treatment of crude tall oil with formaldehyde and sulfuric acid at an average of 125 °C for 1 h, which was found essential to obtain a colorless final product. Then, the product is added to additional crude tall oil and oxidized formic acid and 50 wt% aqueous hydrogen peroxide in hexane under reflux for 2 h. Aqueous by-products were separated by liquid-liquid extraction, and the organic phase was distilled at 60-70 °C under reduced pressure (5-10 mmHg) yielding liquid crude epoxidized fatty acids and solid cross-linked fatty acids by-products. A 99% yield of epoxide was assumed.

The process considered for glyceraldehyde synthesis was a Fenton oxidation of glycerol.[30] Glycerol is oxidized in water in the presence of iron(II) sulfate heptahydrate, sulfuric acid, and 6 wt% H_2O_2 at 5 °C for 6 h and refrigerated for 24 h. The solution is then neutralized with excess calcium carbonate generating calcium carbonate and sulfate waste. Crude glyceraldehyde is obtained with 85.6 % yield.

For biodiesel synthesis, the typical base-catalyzed triglycerides transesterification with methanol, liquid-liquid separation, acidification, and separation of glycerol and unreacted fatty acids followed for the experimental part of this work was considered.[31]

LCIA was conducted on OpenLCA with the Ecoinvent v3.8 database. Assessed impact categories included land use, global warming potential (GWP), ozone depletion, fossil depletion, freshwater ecotoxicity, freshwater eutrophication, land acidification, and water depletion. The ReCiPe Midpoint – H method was employed for all product systems. The provider for each flow was the associated global market, with cutoff, unless otherwise specified in the inventory table (Tables S13-16). The impact of iCALB was assessed through a custom flow process for iCALB production based on LCIA reported for analogous immobilized enzymes (Table S17).[32] Impact analysis was initially performed on a 100 g epoxidized fatty acid scale. Then, a 1 kg scale was considered by scaling up all flows except the electricity needed for the synthesis of the photocatalyst, as that accounted for a major portion of GWP and other categories, as evidenced by the hotspot analysis in **Figure 5b**. The impact was assessed with the energy source for electricity generation either coming natural gas combustion or renewables.

Uncertainty analysis was performed via Monte Carlo simulation with 100 iterations. Uncertainty factors to each flow were assigned using the semiquantitative pedigree matrix as defined by Frischknecht *et al.*,[33] using the score rubric in Table S18 and the pedigree matrix in Table S19. Geometric standard deviations for each flow reported in Table S20 were assigned as the average geometric standard deviations of each score category (reliability, completeness, temporal correlation, geographical correlation, further technological correlation). Lognormal normal distribution was assumed. Geometric standard deviations for the total impact of the three individual process of decentralized fatty waste valorization were calculated with the following equation:[34]

$$\delta Q = \sqrt{\sum_i (\delta_i)^2}$$

Where δQ is the geometric standard deviation of the sum of the invidual standard geometric deviations δ_i.

Sensitivity analysis was conducted for selected parameters with the highest contributions as evidenced by the hotspot analysis reported in **Figure 5b**. For each selected parameter, optimistic and pessimistic cases were designed and justified according to experimental results or projected technical capabilities, as summarized in Table S22. Both continuously variable parameters (e.g. recyclability cycles) and point parameters (e.g. replacement of a flow process) were considered.

A simplified comparative techno-economic analysis was performed to assess the relative gain of a traditional biodiesel synthesis plant and a facility for full fatty waste valorization, including upcycling of unreacted fatty acids and glycerol. To compare the two processes, only costs and revenues relative to a conventional biodiesel synthesis process were considered. Thus, for the integrated domino valorization of fatty waste, only inputs and emissions additional to those pertaining only biodiesel synthesis were considered. Inputs and outputs with relative costs, revenues, and references are reported in Table S25. Reported economic values were obtained from European suppliers and the currency was converted to dollars as a universal metric, using currency conversion factors 1 £ = 1.34 $ and 1 € = 1.16 $ as of August 2025.

Relative costs and revenues were calculated for the production of 1 kg of epoxidized fatty acids, 1.52 kg of glyceraldehyde, and 62.9 kg of biodiesel. Temporal parameters such as plant lifetime and solar irradiation time were not considered, as we thought mass normalization of economic values was sufficient for the comparative purposes of this simplified analysis. Relative return on investment (ROI) was calculated as the ratio between relative costs and revenues. To account for scaling, retail prices obtained by suppliers were amortized according to the equation:[35]

$$\frac{C_1}{C_2} = \left(\frac{w_1}{w_2}\right)^{0.6}$$

Where C_1 and C_2 are the economic values of a material at a scale w_1 and w_2.

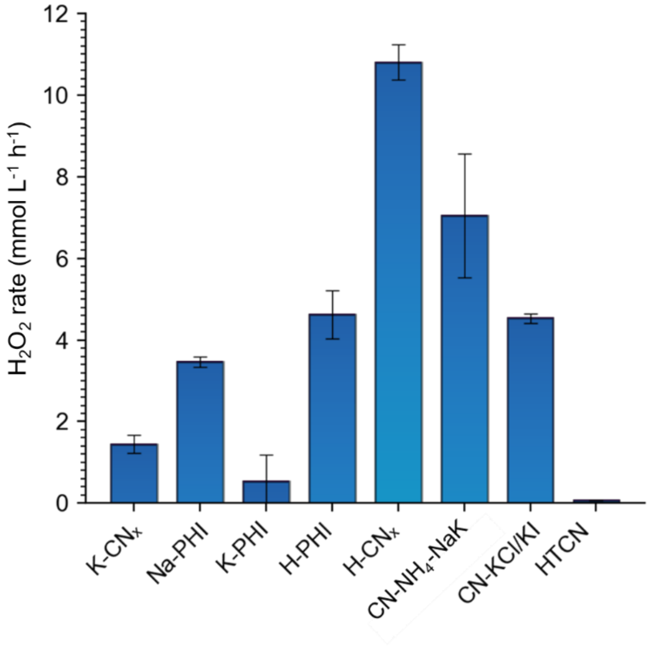

Figure S1 | Screening of CN_x-based photocatalyst for H_2O_2 synthesis from ORR with aqueous glycerol as the electron donor. Reaction conditions: catalyst (5 mg), aqueous glycerol (50 wt%, 2 mL), O_2 (1 atm), 450 nm (40±4 mW cm^{-2}), 25 °C.

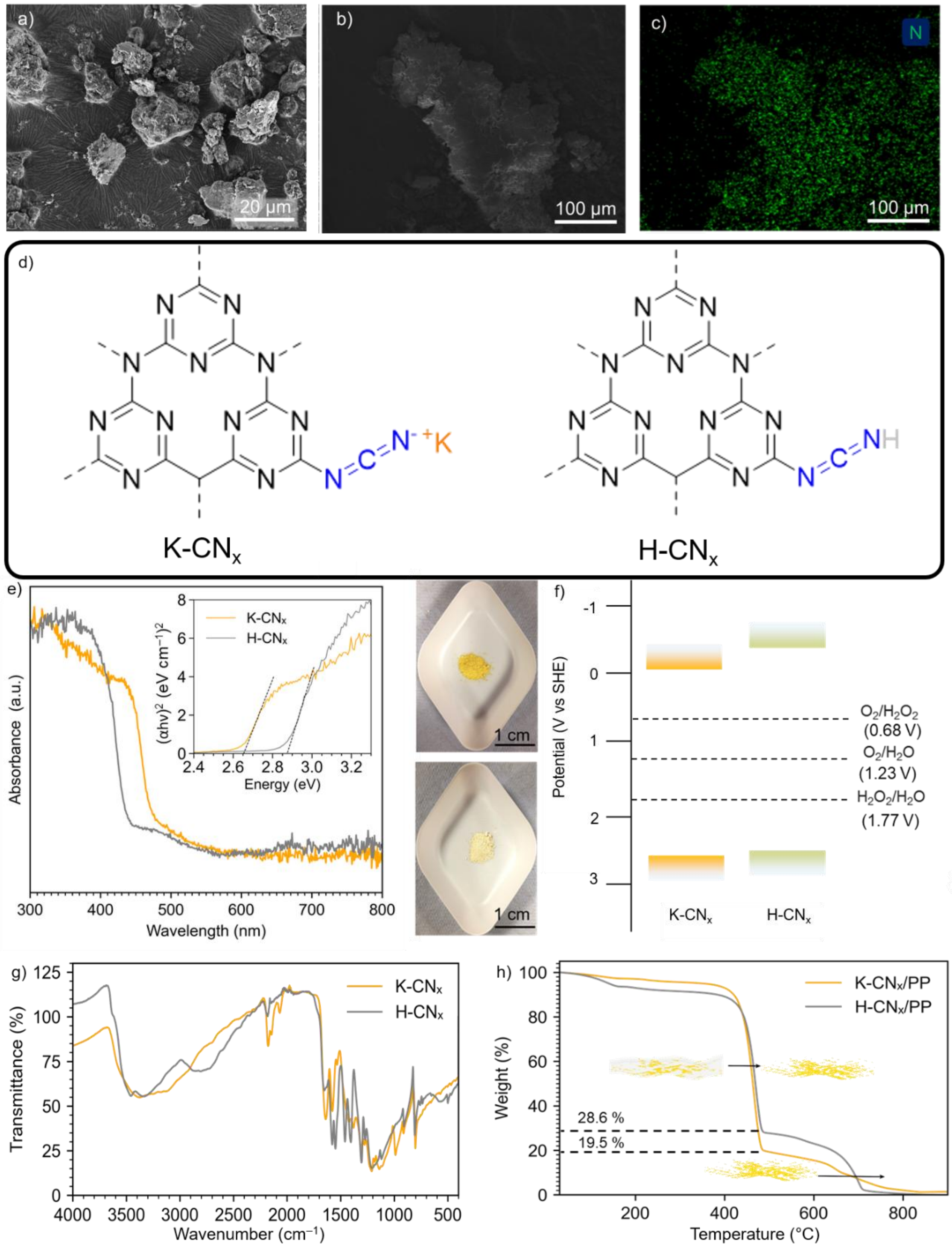

Figure S2 | a,b) SEM images of H-CN_x/PP. c) EDX N Kα1 EDX mapping of H-CN_x/PP. d) Chemical structure of the repeating heptazine units and cyanamide side groups of K-CN_x and H-CN_x. e) Diffuse reflectance UV-Vis of K-CN_x and H-CN_x (inset: extrapolated Tauc plots. The dashed lines indicate a bandgap of ~2.65 eV for K-CN_x and ~2.87 eV for H-CN_x). Pictures on the right show K-CN_x (top) and H-CN_x (bottom) powders. f) Extrapolated band edge positions of K-CN_x and H-CN_x. Redox potentials vs SHE of relevant ORR and H_2O_2 reduction couples are indicated with dashed lines for comparison. g) ATR-IR and of K-CN_x and H-CN_x. h) TGA traces (under N_2) of K-CN_x/PP and H-CN_x/PP. Dashed lines mark the weight loss from plastic and indicate the approximate loading of CN_x. Calculation details in Supplementary Methods.

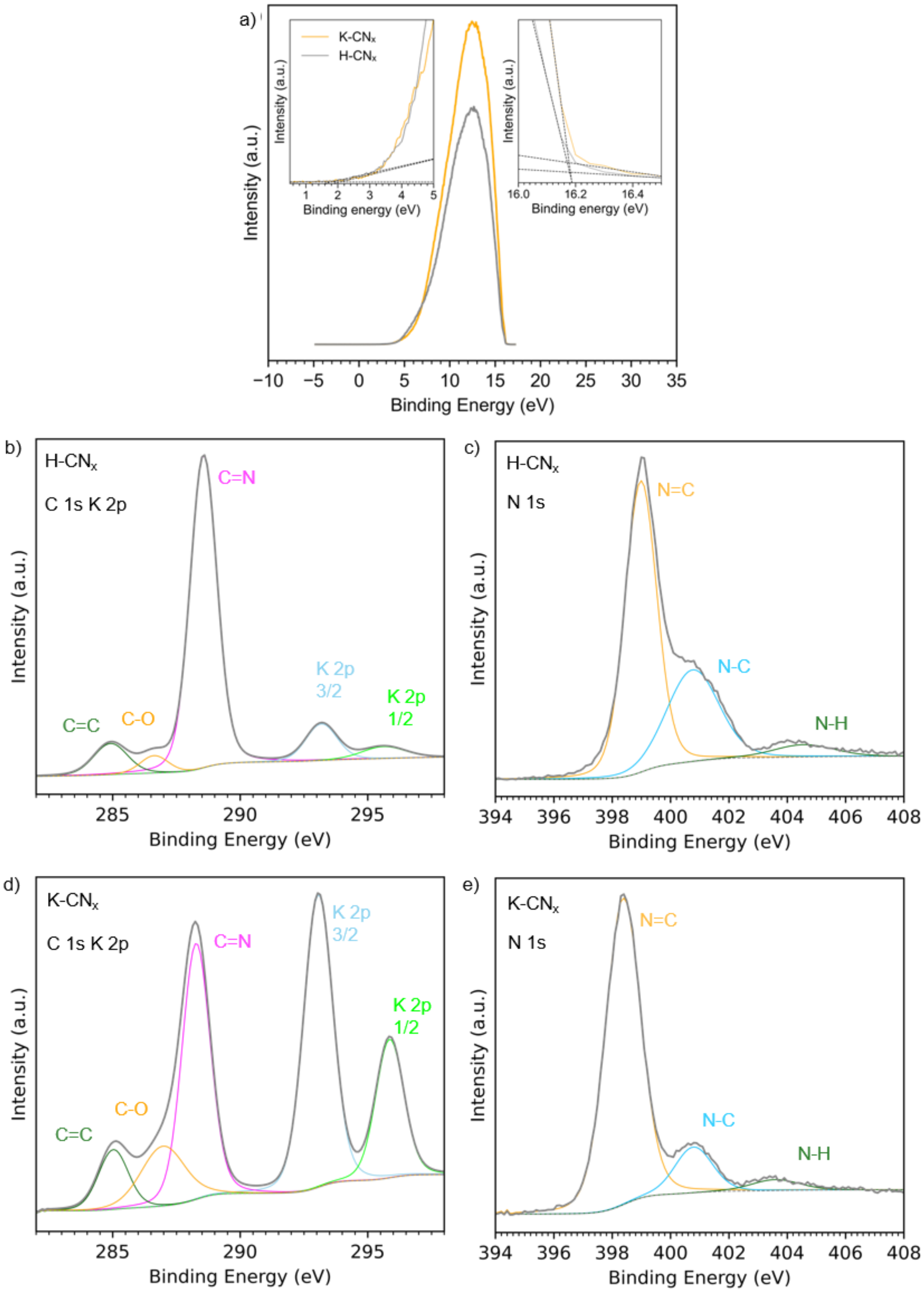

Figure S3 | a) UPS analysis of K-CN$_x$ and H-CN$_x$. Left inset: determination of the energy difference between the valence band edge and the Fermi level. Right inset: determination of the secondary electron cutoff energy. b) XPS analysis. of K-CN$_x$ and H-CN$_x$. (b) C 1s and K 2p, (c) N 1s edge XPS spectra of H-CN$_x$. (d) C 1s and K 2p, (e) N 1s edge XPS spectra of K-CN$_x$.

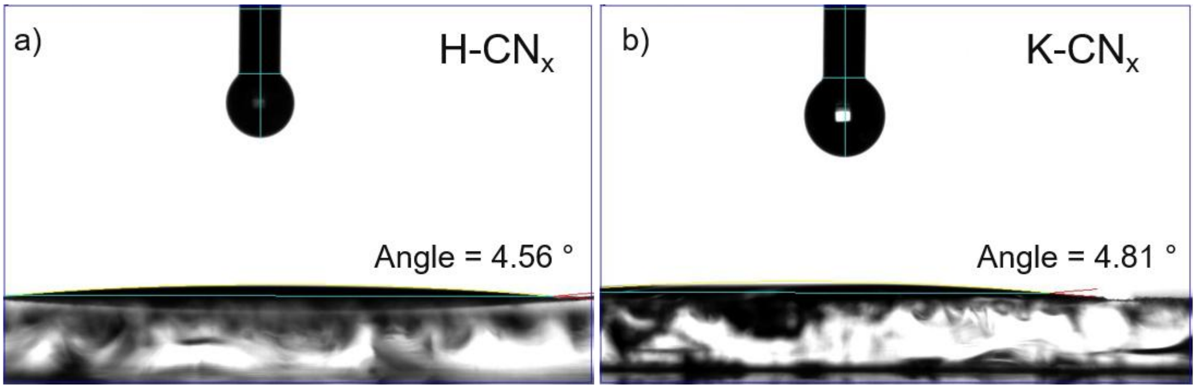

Figure S4 | Contact angle of a) K-CN$_x$ and b) H-CN$_x$ films spray-coated on glass.

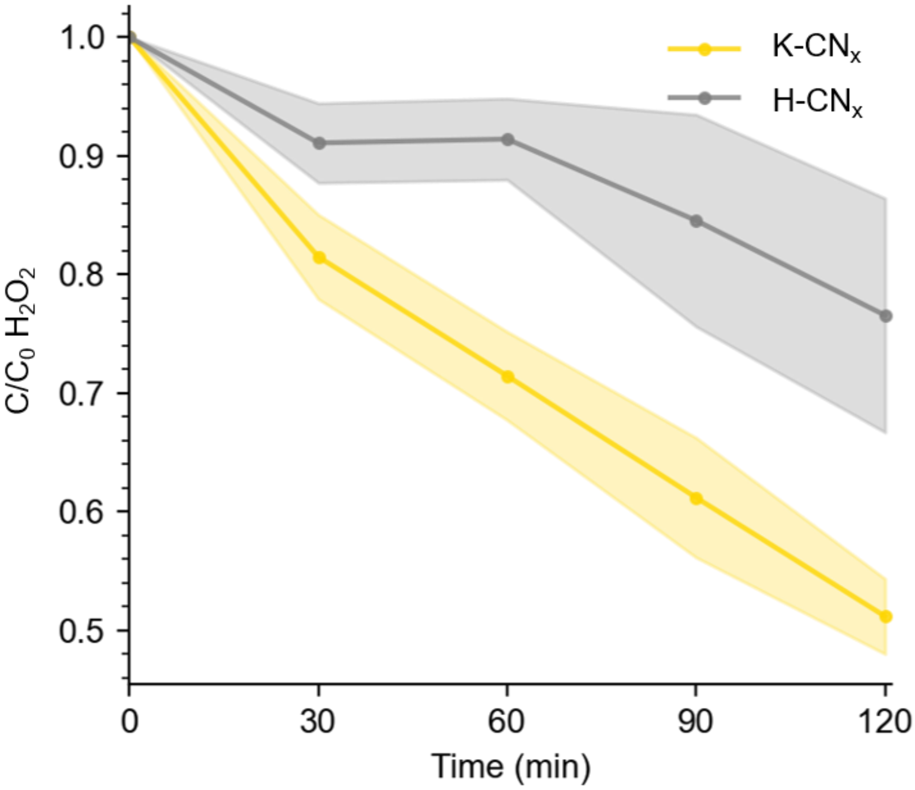

Figure S5 | b) Kinetics of photocatalytic H_2O_2 decomposition in the presence of K-CN$_x$ or H-CN$_x$. Reaction conditions: catalyst (2 mg), aqueous H_2O_2 (0.020 mmol, 10 mM, 2 mL), N_2 (1 atm), 450 nm (40±4 mW cm^{-2}), 25 °C.

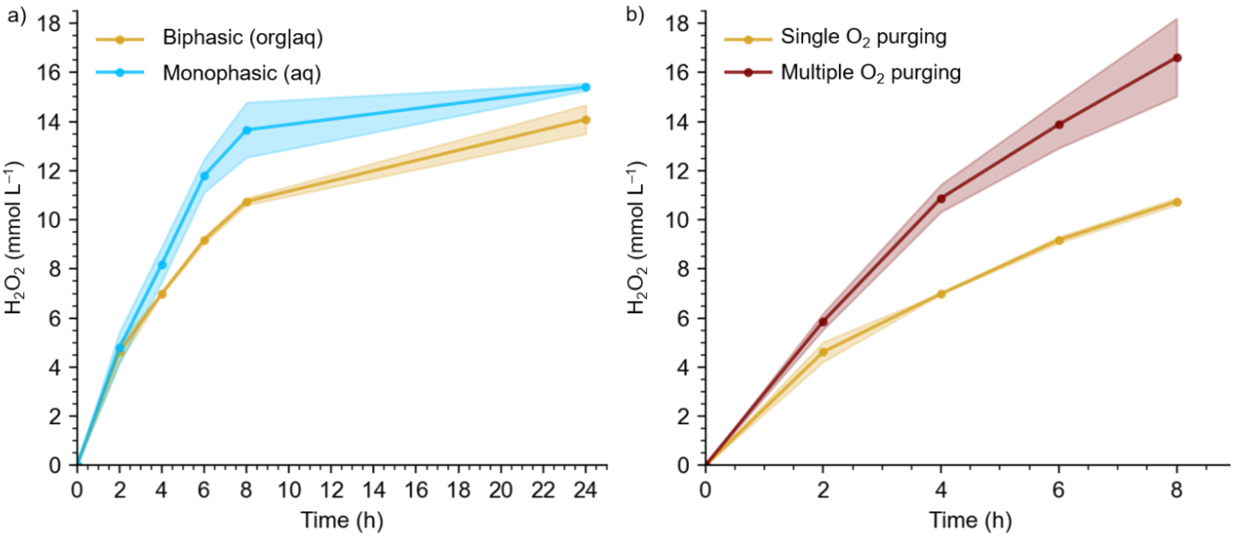

Figure S6 | a) Photocatalytic H_2O_2 evolution in biphasic organic|aqueous and monophasic aqueous conditions. Reaction conditions: aqueous glycerol (30 wt%, 2 mL), H-CN_x/PP (20 mg), O_2 (1 atm), 450 nm (40±4 mW cm^{-2}). Ethyl acetate (2 mL) was added in biphasic conditions. b) Photocatalytic H_2O_2 evolution in organic|aqueous mixture with single and multiple O_2 purging. Reaction conditions: aqueous glycerol (30 wt%, 2 mL), ethyl acetate (2 mL), H-CN_x/PP (20 mg), O_2 (1 atm, purged only for 5 min before the experiment, or 5 min every 2 h), 450 nm (40±4 mW cm^{-2}).

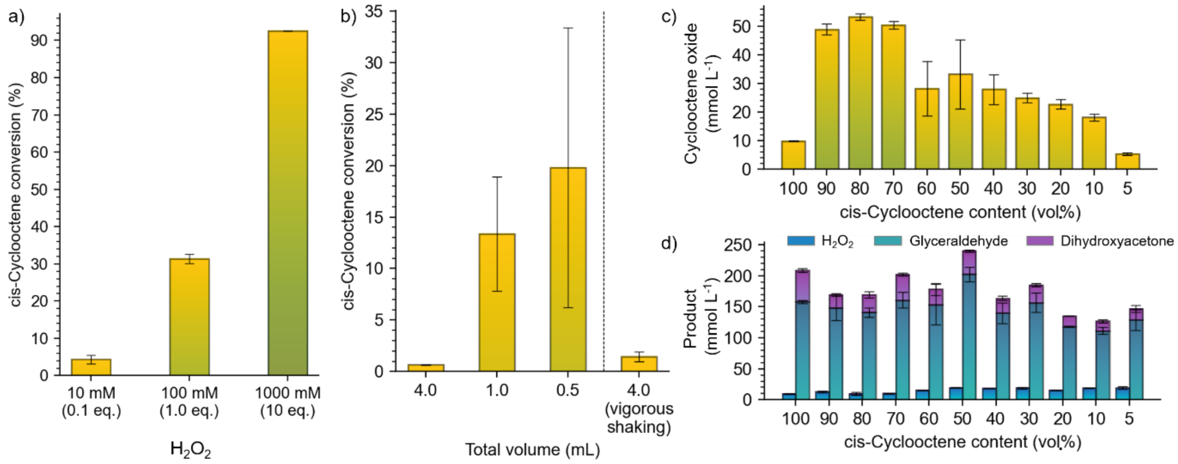

Figure S7 | Evaluation of conditions needed to achieve high alkene-to-epoxide conversion in the macroscopic liquid|solid|liquid system with cis-cyclooctene as a model substrate. a) Effect of aqueous H_2O_2 concentration, b) Effect of the ratio between liquid volume and liquid-liquid interface surface. Reaction conditions: a) iCALB (40 mg), aqueous H_2O_2 (2 mL), cis-cyclooctene (0.2 mmol) in ethyl acetate (2 mL), 40 °C, 16 h. b) H-CN_x/PP (20 mg), 1:1 aqueous/organic volume ratio, O_2 (1 atm), 450 nm (40±4 mW cm^{-2}), 40 °C, 24 h. Vials were typically shaken at 250 rpm. Vigorous shaking was realized at a speed of 450 rpm. c,d) Optimization of alkene concentration in the organic phase for domino photochemo-enzymatic epoxidation of the model substrate cis-cyclooctene, showing the amount of product generated in c) the organic and d) the aqueous phase. Product concentrations refer to the volumes of the corresponding phases. Reaction conditions: H-CN_x/PP (20 mg), iCALB (40 mg), aqueous glycerol (30 wt%, 2 mL), cis-cyclooctene in ethyl acetate (2 mL), O_2 (1 atm), 450 nm (40±4 mW cm^{-2}), 40 °C, 24 h.

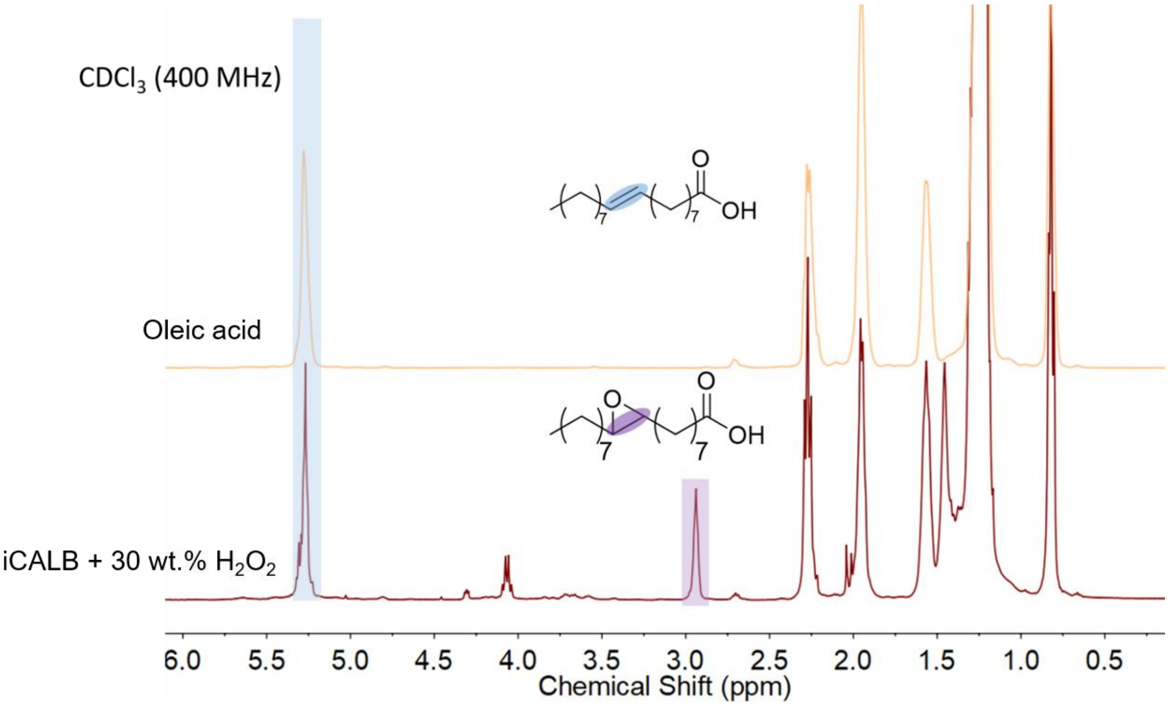

Figure S8 | ^{1}H-NMR (CDCl$_3$, 400 MHz) of pristine oleic acid (top) and a solution of oleic acid in ethyl acetate treated with 40 mg iCALB and 30 wt% aqueous H_2O_2 (bottom).

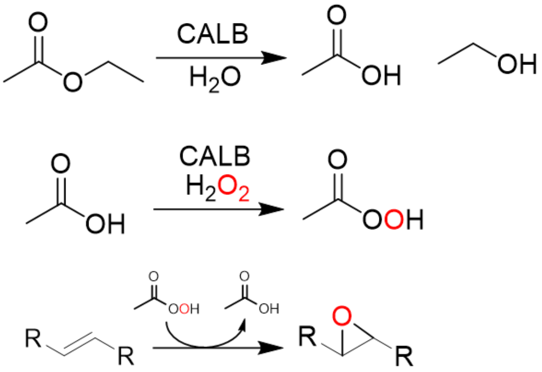

Figure S9 | Scheme of the contribution of ethyl acetate in iCALB-catalyzed alkene epoxidation with H_2O_2.

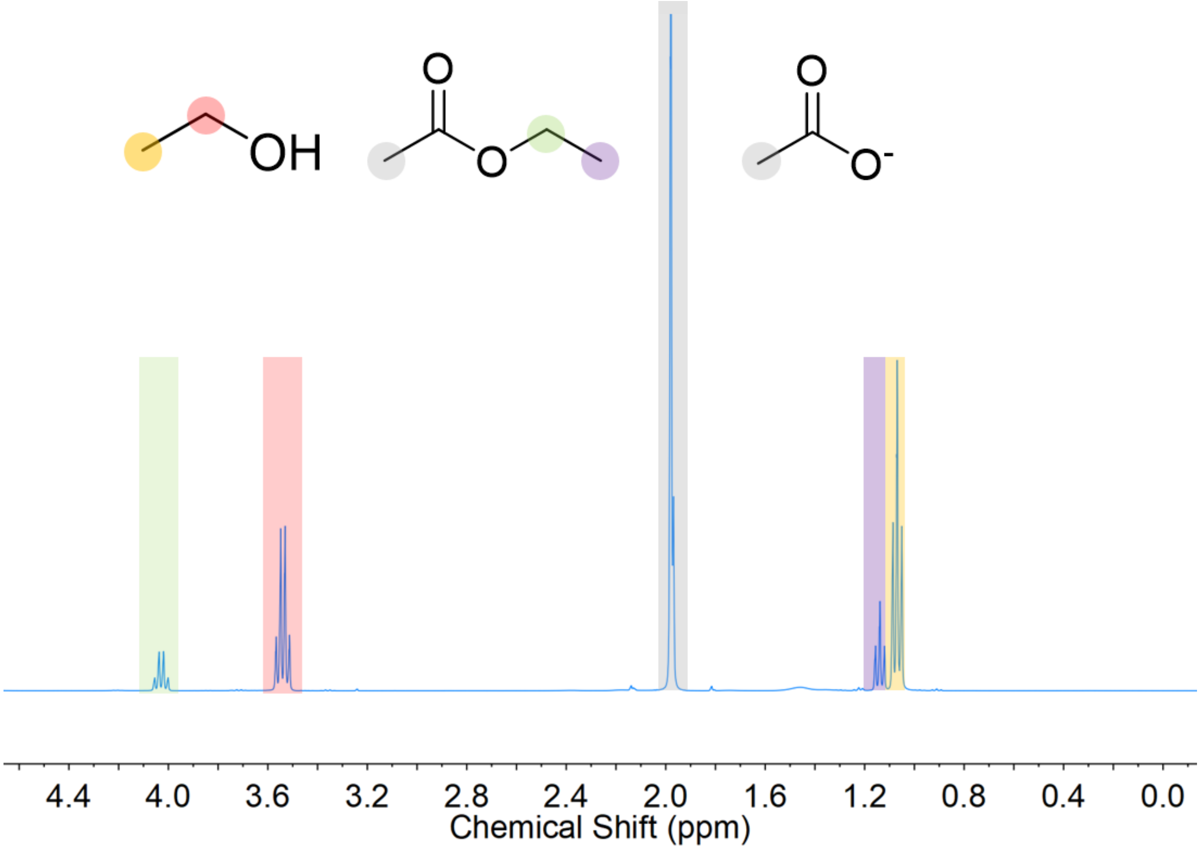

Figure S10 | ^1H-NMR spectrum (D_2O, 400 MHz), of aqueous phase recovered after 16 h photoreaction in a mixture of ethyl acetate, H-CN_x/PP iCALB and deionized water, showing the presence of ethanol from iCALB-catalyzed ethyl acetate hydrolysis and traces of ethyl acetate. Reaction conditions: 20 mg H-CN_x/PP, 40 mg iCALB, deionized water (30 wt%, 2 mL), ethyl acetate (2 mL), 450 nm (40±4 mW cm^{-2}), 25 °C, 16 h.

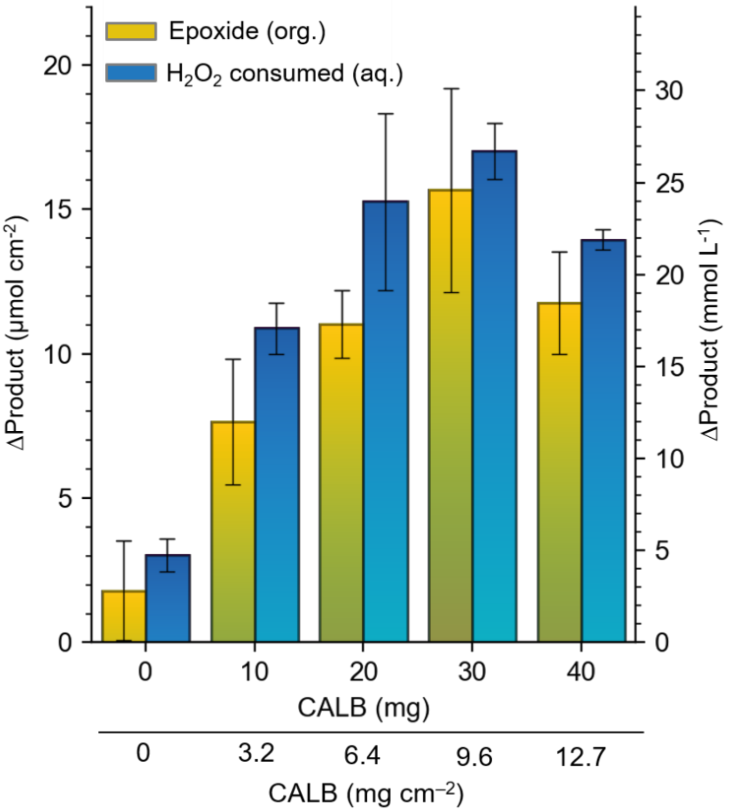

Figure S11 | a) Optimization of iCALB loading for the enzymatic epoxidation of oleic acid with H_2O_2. Reaction conditions: iCALB, aqueous H_2O_2 (40 mM, 2 mL), oleic acid in ethyl acetate (40 wt% in 2 mL), 25 °C, 16 h.

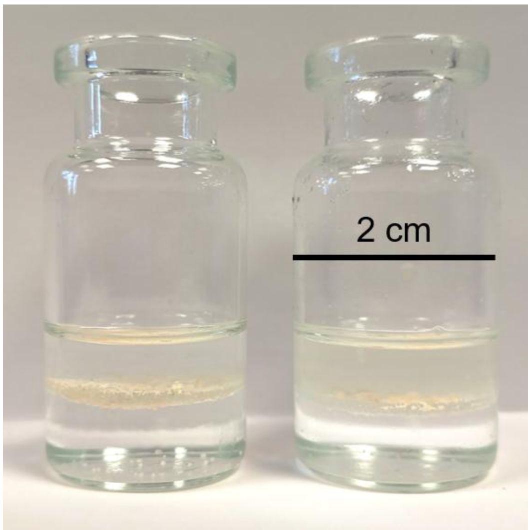

Figure S12 | Picture of the liquid|solid|liquid system comprising aqueous glycerol, floating H-CN_x/PP and iCALB, and oleic acid in ethyl acetate freshly prepared (left) and after 10 photocatalytic runs (1 h each) each followed by the replacement of the aqueous and organic phases.

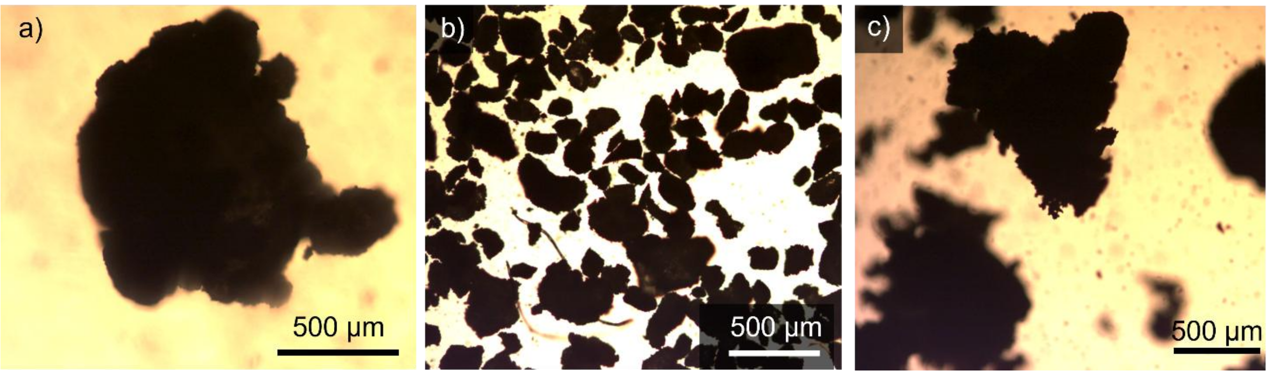

Figure S13 | Optical microscope images of H-CN$_x$/PP composite as fabricated (a) and after cryogenic treatment with liquid N_2 immediately followed by mechanical grinding (b), and recovered after 6 days continuous operation under 420 nm irradiation (c). Full reaction conditions used for particles collected in (c): aqueous glycerol (30 wt%, 2 mL), oleic acid in ethyl acetate (40 wt%, 2 mL), H-CN$_x$/PP (20 mg), iCALB (40 mg), O_2 (1 atm), 450 nm (25 mW cm^{-2}), 25°C, 6 days).

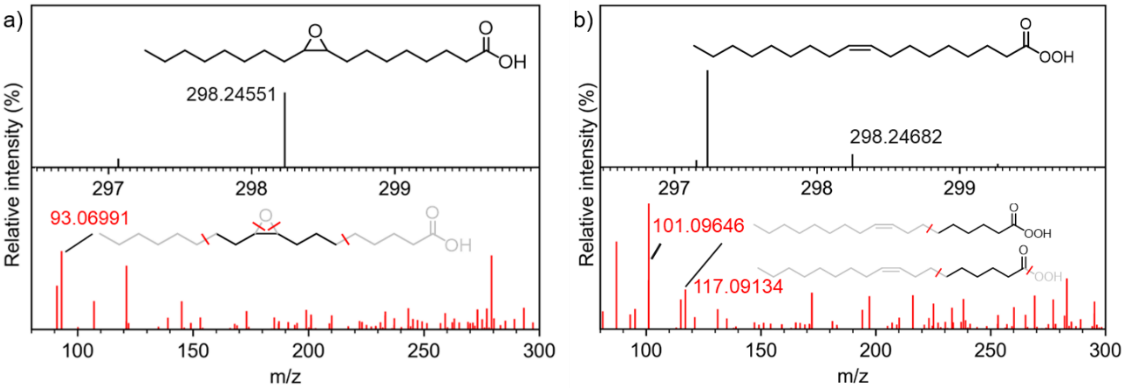

Figure S14 | Accurate mass spectra (top) and tandem MS-MS spectra of the peak indicated on the top (bottom) of LC-MS analysis of a) 9,10-epoxystearic and b) peroxyoleic acid.

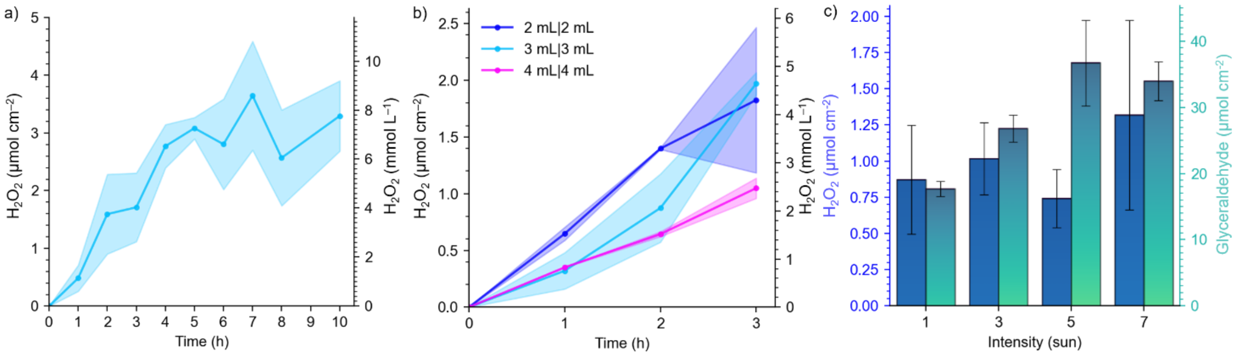

Figure S15 | a) Extended kinetics of photocatalytic H_2O_2 production under simulated solar light. Reaction conditions: H-CN$_x$/PP (50 mg), aqueous glycerol (30 wt%, 3 mL), oleic acid in ethyl acetate (40 wt%, 3 mL), O_2 (1 atm), simulated solar light (AM 1.5G, 100 mW cm^{-2}, 1 sun). b) Concentration of H_2O_2 evolved from photocatalytic ORR under simulated solar light at different aqueous|organic phase volume ratios. Reaction conditions: H-CN$_x$/PP (50 mg), aqueous glycerol (30 wt%), oleic acid (40 wt%) in ethyl acetate, O_2 (1 atm), simulated solar light (AM 1.5G, 100 mW cm^{-2}, 1 sun). c) Screening of simulated solar light intensity for H_2O_2 synthesis from ORR coupled with glycerol oxidation photocatalyzed by the floatable H-CN$_x$/PP composite. Reaction conditions: H-CN$_x$/PP (50 mg), aqueous glycerol (30 wt%, 2 mL), oleic acid in ethyl acetate (40 wt%, 2 mL), O_2 (1 atm), simulated solar light irradiation concentrated with a Fresnel lens (XL Full Page, 3x magnification, PVC), 2 h.

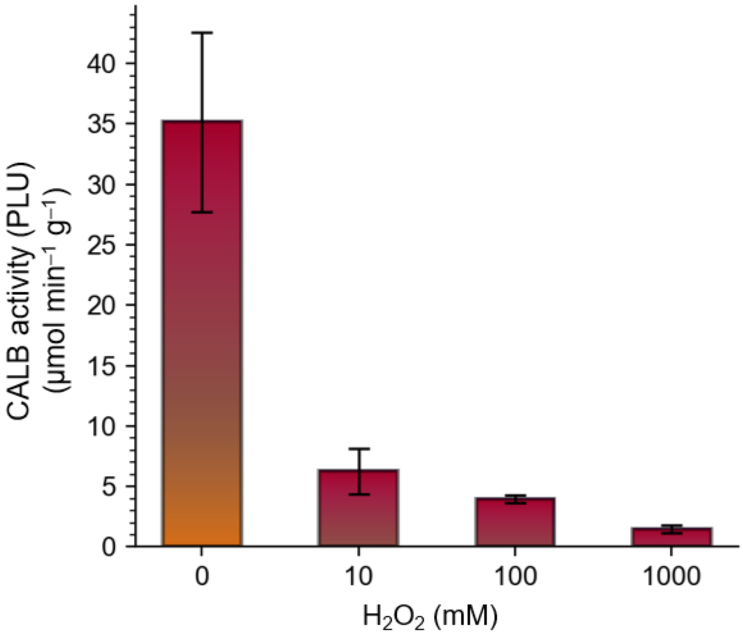

Figure S16 | Effect of aqueous H_2O_2 concentration on iCALB deactivation. Reaction conditions: 20 mg of iCALB were added to an aqueous H_2O_2 solution (2 mL) and shaken (250 rpm) at 37 °C for 24 h. Afterward, iCALB was filtered, washed with ethyl acetate, dried and stored overnight at 4 °C. Then, 10 mg of iCALB was added to a solution of lauric acid (0.100 mmol, 100 mM) in 1-propanol (1 mL), and stirred for 30 min at 25 °C. The activity was assessed from the amount of propyl laurate produced as Propyl Laurate Units (details in Supplementary Methods).

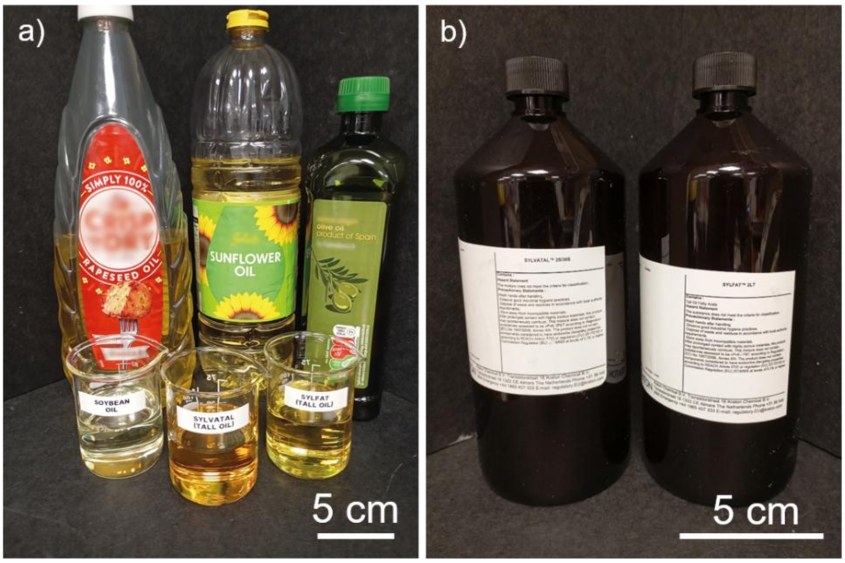

Figure S17 | Pictures of a) commercial vegetable oils and tall oil samples and b) tall oil samples provided by Kraton® used in this work.

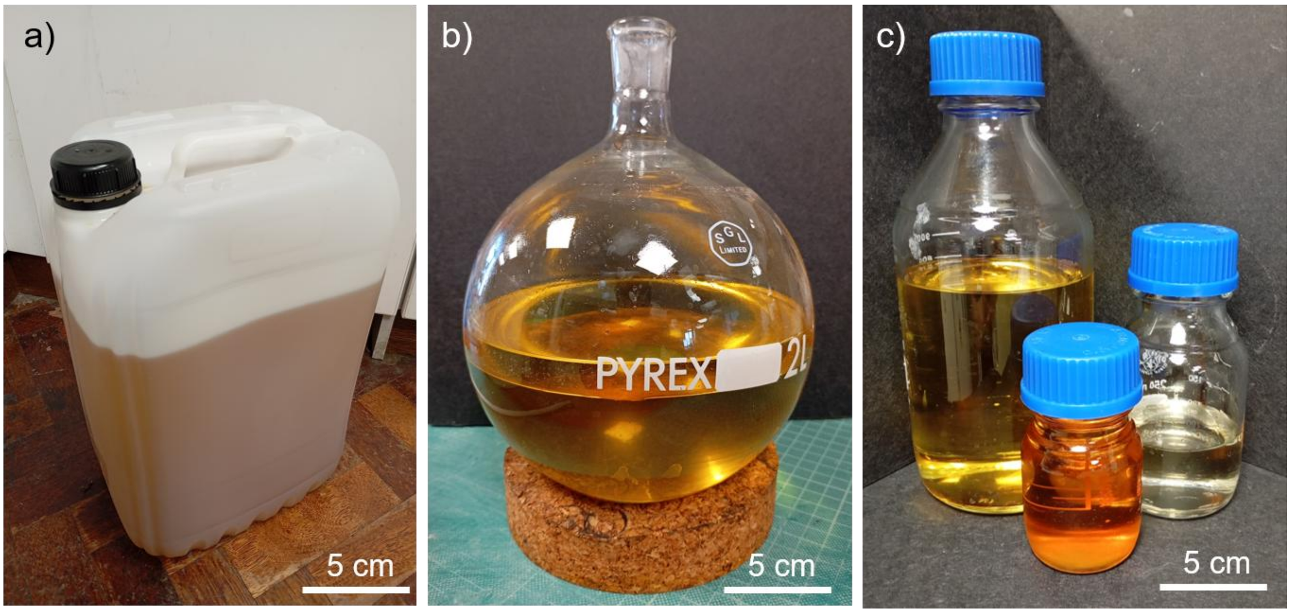

Figure S18 | a) Picture of used vegetable oil collected from a local kitchen. b) Picture of mixture obtained from 1 L scale biodiesel synthesis with used vegetable oil. c) Pictures of (from left to right) biodiesel, unreacted fatty acids and glycerol fractions obtained from 1 L of used vegetable oil.

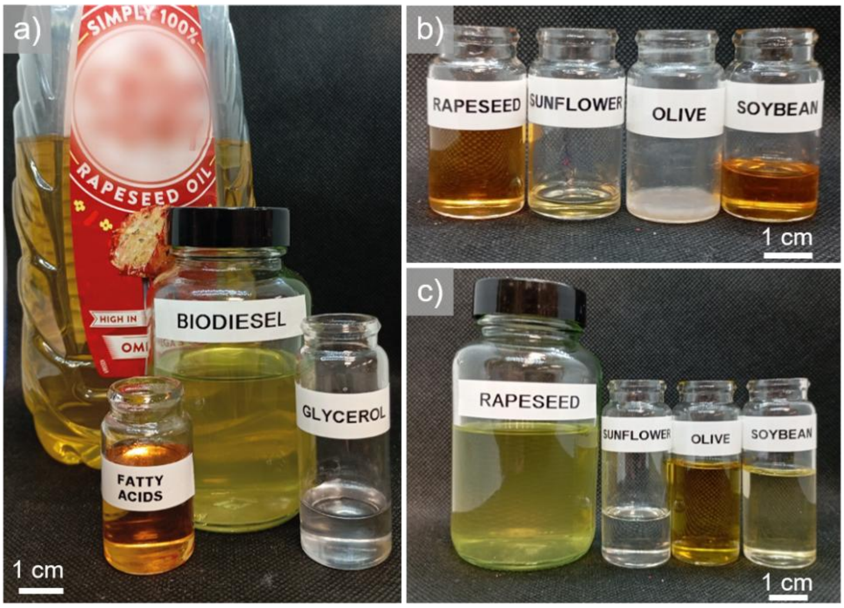

Figure S19 | a) Picture of biodiesel, unreacted fatty acids and glycerol fractions collected from commercial rapeseed oil. Pictures of b) Unreacted fatty acids and c) biodiesel fractions collected from commercial vegetable oils.

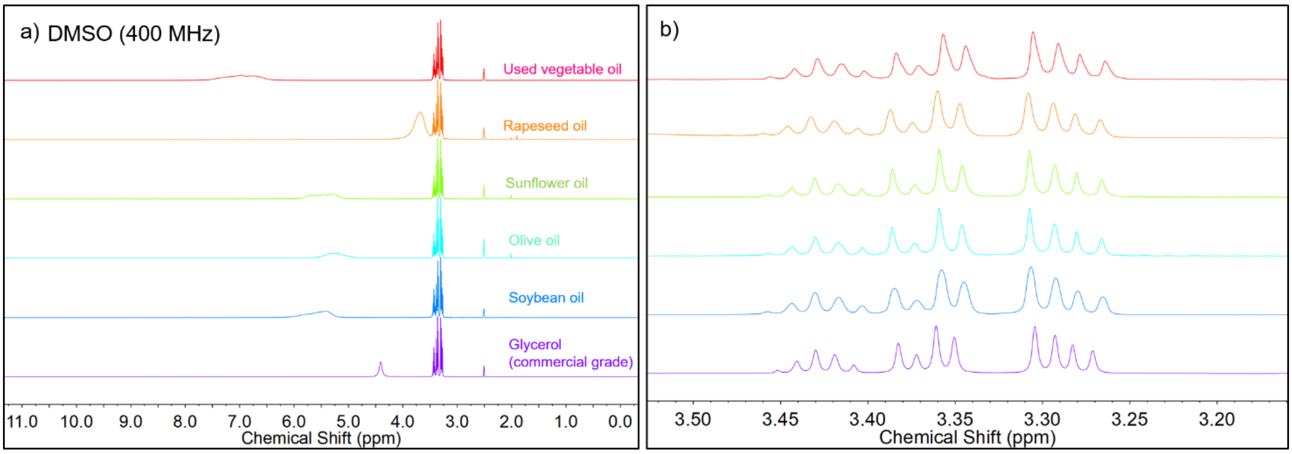

Figure S20 | a) ^{1}H-NMR (DMSO, 400 MHz) spectra of glycerol fractions obtained from used and commercial vegetable oils. Pure glycerol (purple trace at the bottom) is shown for comparison. Broad signals above 3.5 ppm are attributed to protons from the alcoholic groups. b) Detail of the aliphatic proton signals of the ^{1}H-NMR traces in a).

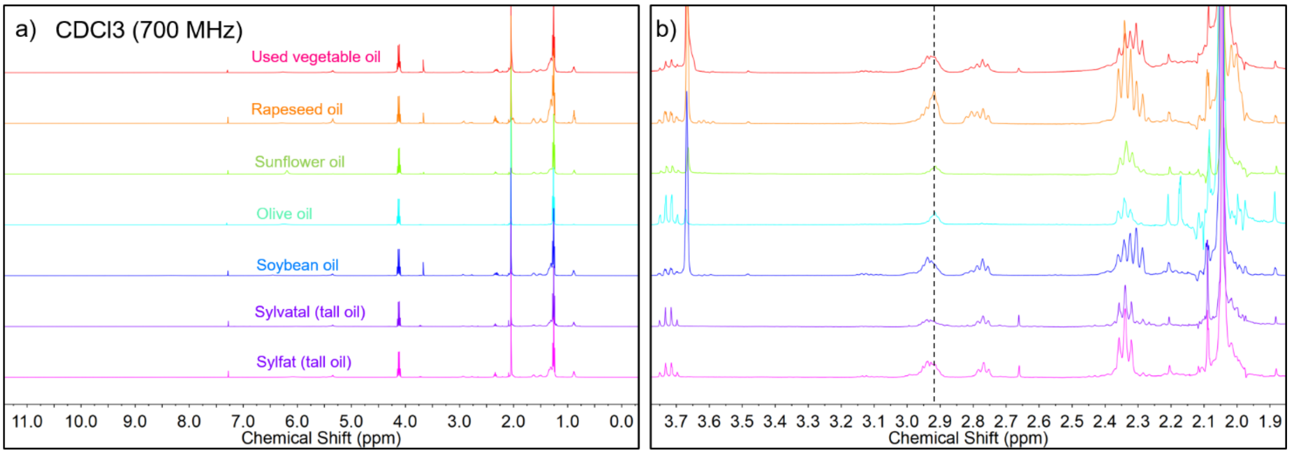

Figure S21 | a) Representative ^{1}H-NMR ($CDCl_3$, 700 MHz) spectra of epoxidized fatty acids obtained from the fractionation of used and commercial vegetable oils and tall oils. b) Details of the aliphatic region of the ^{1}H-NMR traces in a). The dashed line indicates the signal from aliphatic protons in the epoxide ring (~2.9 ppm).

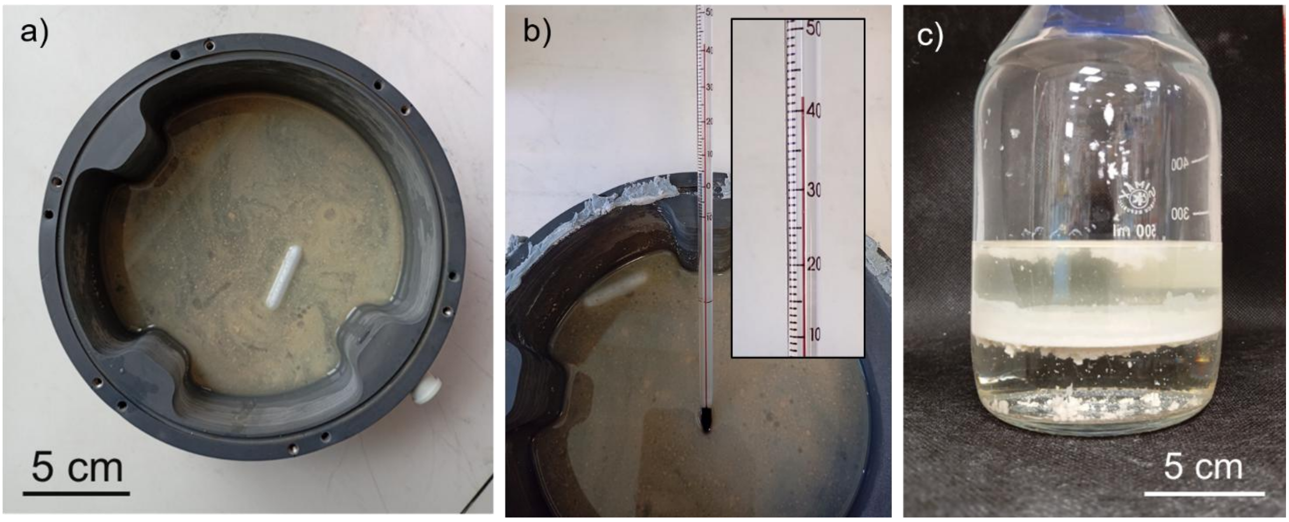

Figure S22 | Pictures of a) 100 mL scale batch reactor, b) temperature of the solution after 2 h irradiation under simulated solar light (AM 1.5G, 100 mW cm^{-2}, 1 sun), with close-up of temperature read by a thermometer showed in the inset, c) liquid|solid|liquid mixture recovered after 2 h of continuous photocatalysis under simulated solar light (AM 1.5G, 100 mW cm^{-2}, 1 sun).

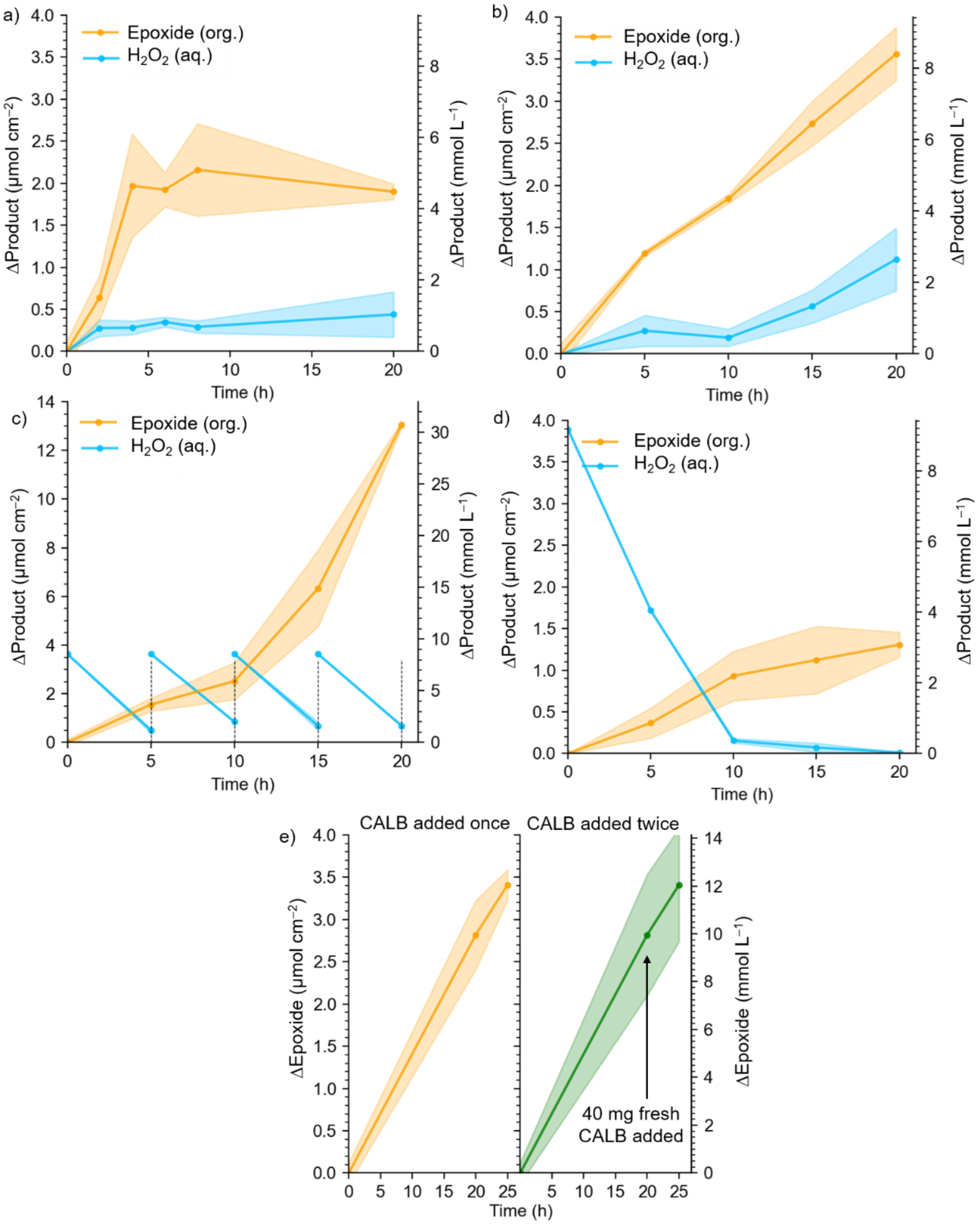

Figure S23 | a) Kinetics of domino photochemo-enzymatic oleic acid epoxidation showing a plateau in the production of epoxide. Reaction conditions: aqueous glycerol (30 wt%, 3 mL), oleic acid in ethyl acetate (40 wt%, 3 mL), H-CN_x/PP (50 mg), iCALB (40 mg), O_2 (1 atm), simulated solar light (AM 1.5G, 100 mW cm^{-2}, 1 sun). b) Effect of replacing the aqueous glycerol phase for the domino photochemo-enzymatic epoxidation of oleic acid. Reaction conditions: as in a), except that the aqueous glycerol phase was replaced every 5 h. c,d) Domino epoxidation with exogeneous H_2O_2 without (c) and with (d) replacement of the aqueous H_2O_2 phase every 5 h. Reaction conditions: as in a), except that H-CN_x/PP was removed and the aqueous glycerol was replaced with aqueous H_2O_2 (0.027 mmol, 9.8 mM, 3 mL). e) Effect of adding fresh iCALB for the domino photochemo-enzymatic epoxidation of oleic acid. Reaction conditions: orange trace: as in a), green trace: 40 mg fresh iCALB were added after 20 h.

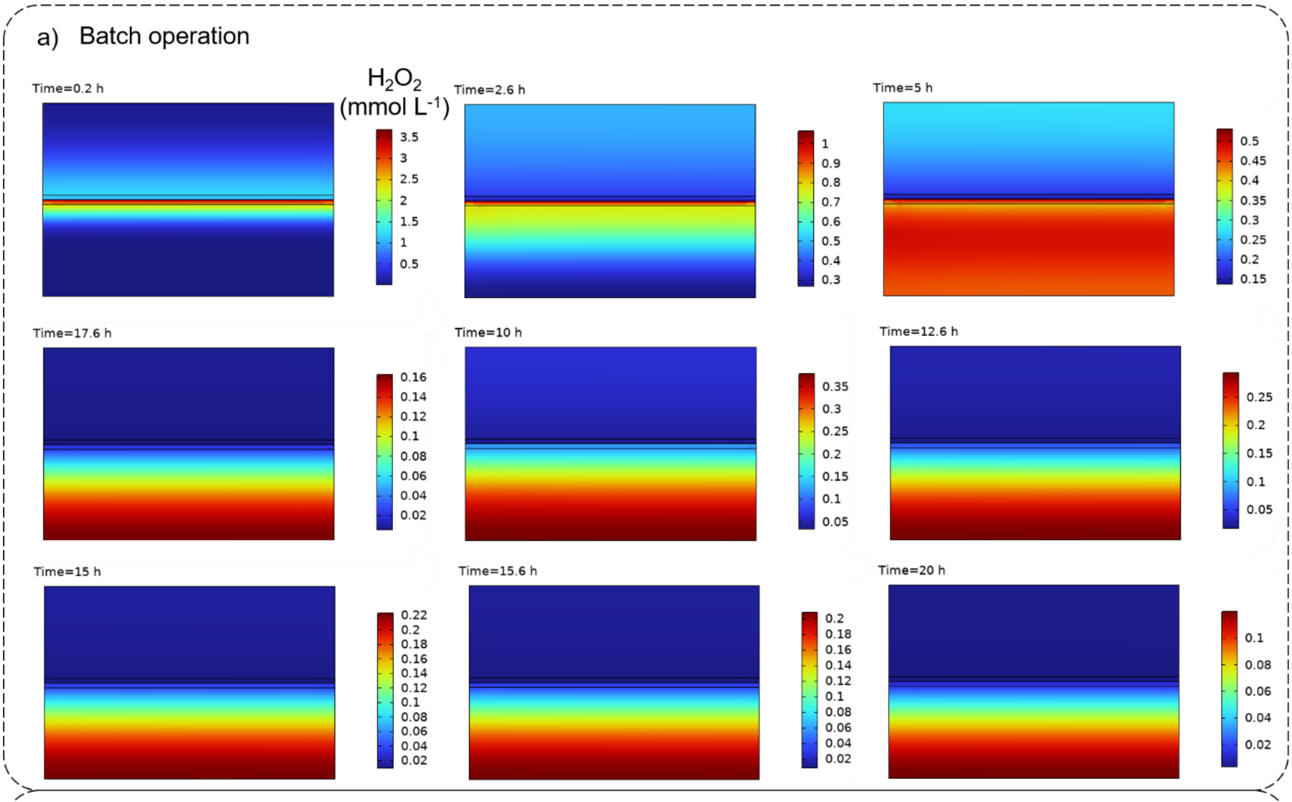
a) Batch operation

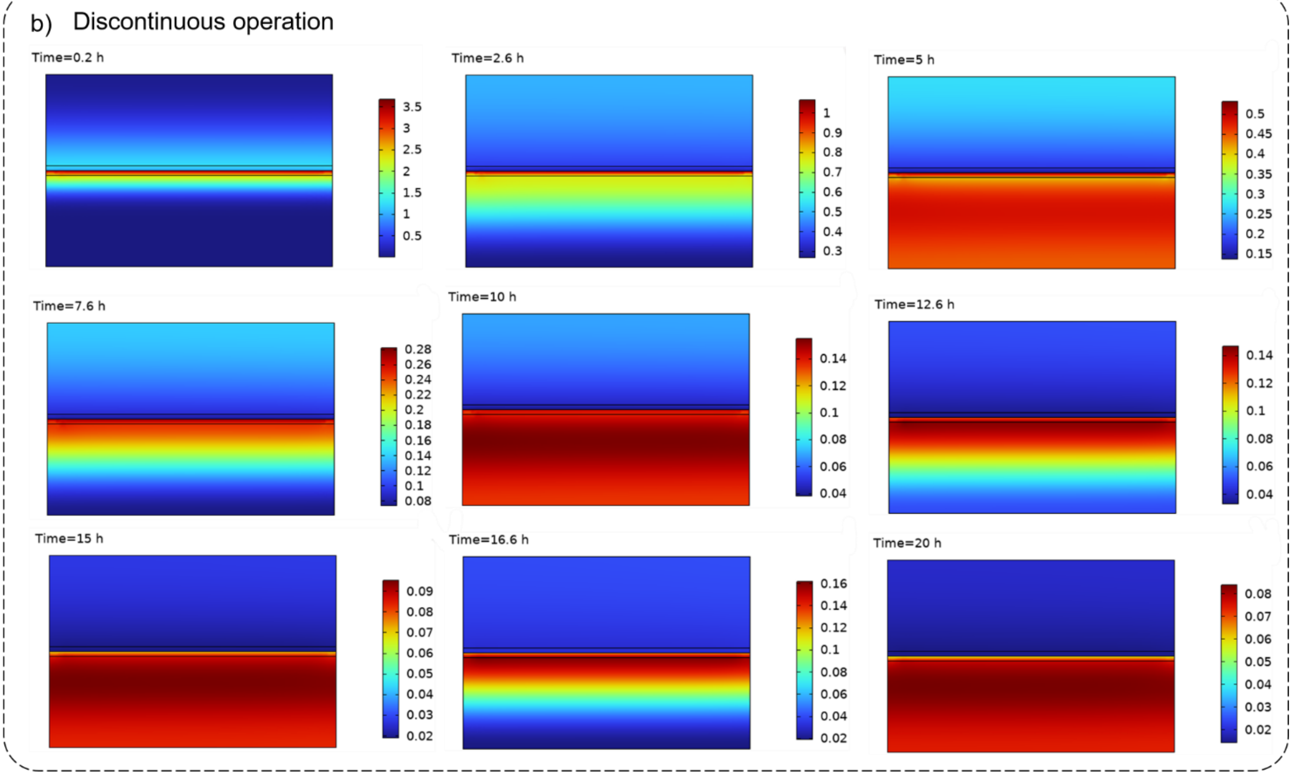
b) Discontinuous operation

Figure S24 | Simulated evolution of H_2O_2 concentration profiles over 20 h reaction under a) batch and b) discontinuous operation. To simulate the periodical replacement of the aqueous phase under discontinuous operation (b), H_2O_2 and O_2 in the bottom (aqueous) compartment were reset to 0 and 1.22 mmol L^{-1} every 5 h, respectively. Additional details on the simulation parameters are reported in Supplementary Note 4.

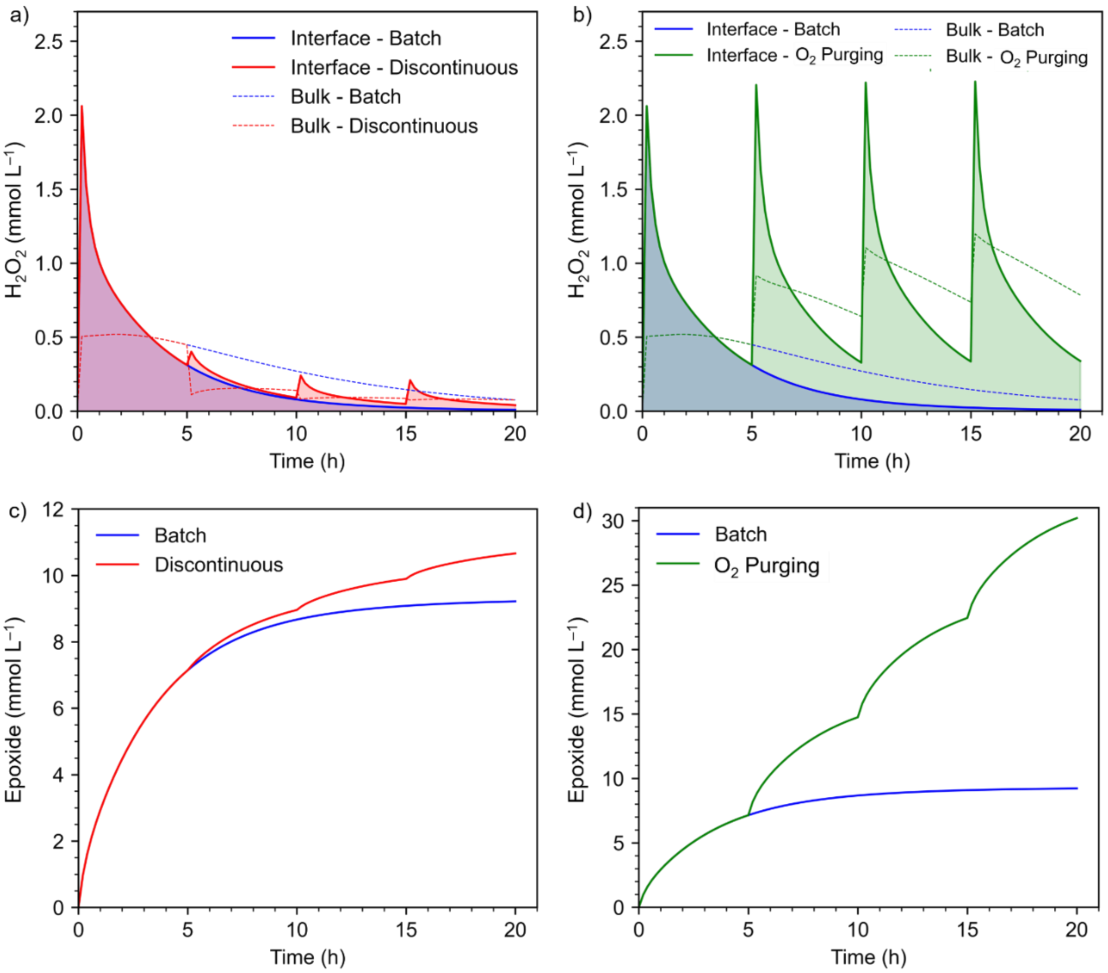

Figure S25 | a,b) Simulated evolution of average H_2O_2 concentration at the interface and in the bulk under a) batch and discontinuous operation with periodical replacement of the aqueous phase, and b) single and periodical O_2 purging operation. The shaded area highlights the total number of moles of H_2O_2 produced at the interface during the reaction, given by the integral of each trace. Interfacial H_2O_2 concentration determines the rate of epoxidation in the organic phase. c,d) Simulated evolution of average epoxide concentration in the bulk of the organic phase under c) batch and discontinuous operation with periodical replacement of the aqueous phase, and d) single and periodical O_2 purging operation.

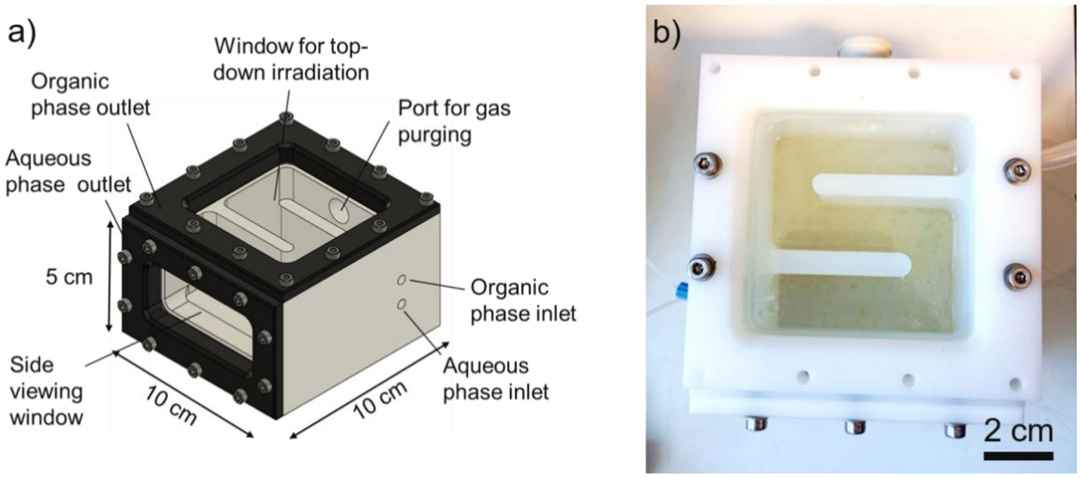

Figure S26 | a) Scheme and b) top view picture of the custom flow photoreactor.

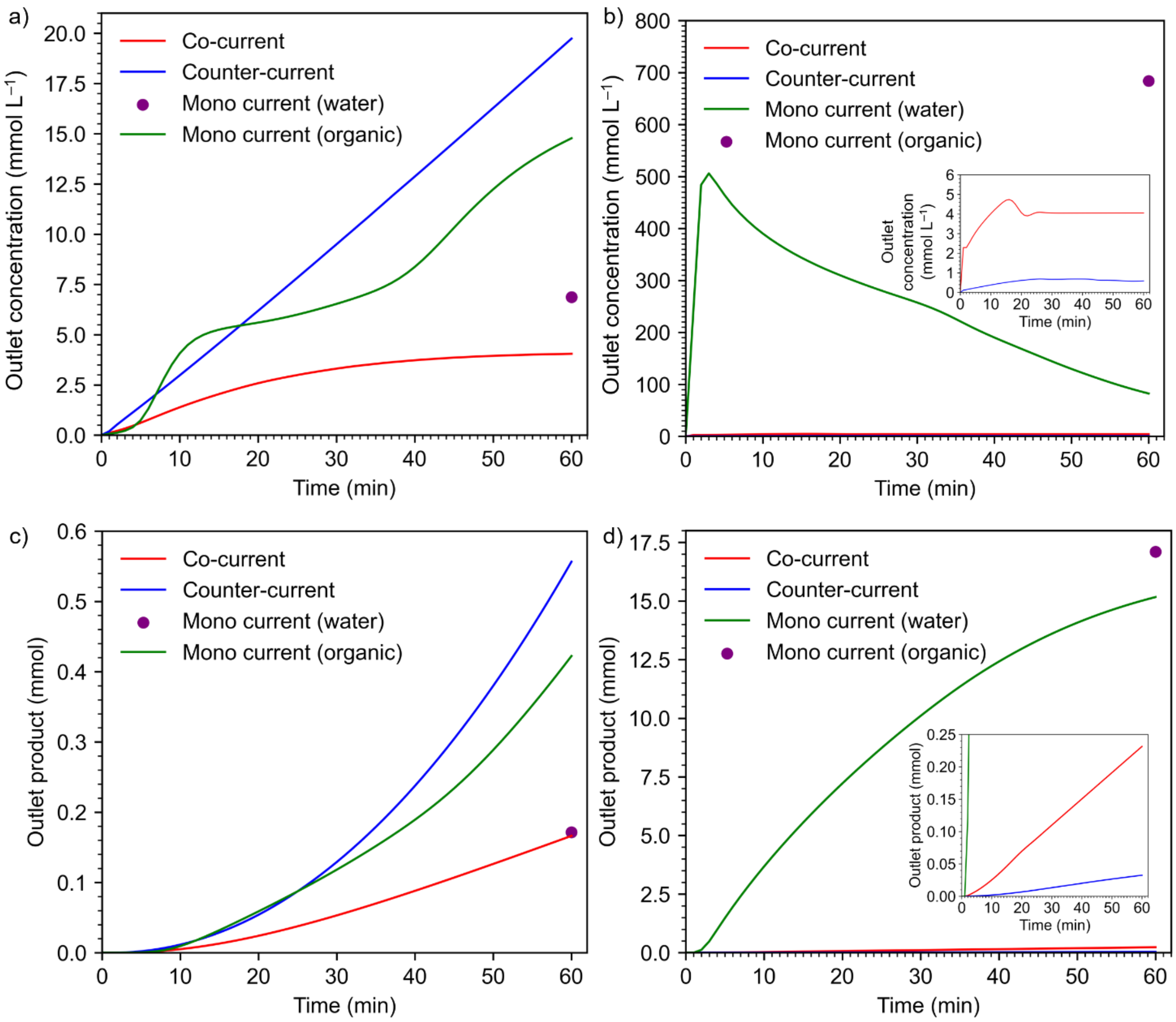

Figure S27 | a,b) Simulated outlet concentrations of (a) epoxide from the upper (organic) compartment and (b) glyceraldehyde from the bottom (aqueous) compartment under different flow operations. For mono flow operation where the major solvent for each substrate (water for glyceraldehyde, organic for epoxide), was kept static, the average concentration in the bulk of the static phase at the end of the sampled period (60 min) was reported (purple point). c,d) Number of moles of (c) epoxide from the upper (organic) compartment and (d) glyceraldehyde from the bottom (aqueous) compartment calculated from (a) and (b), respectively.

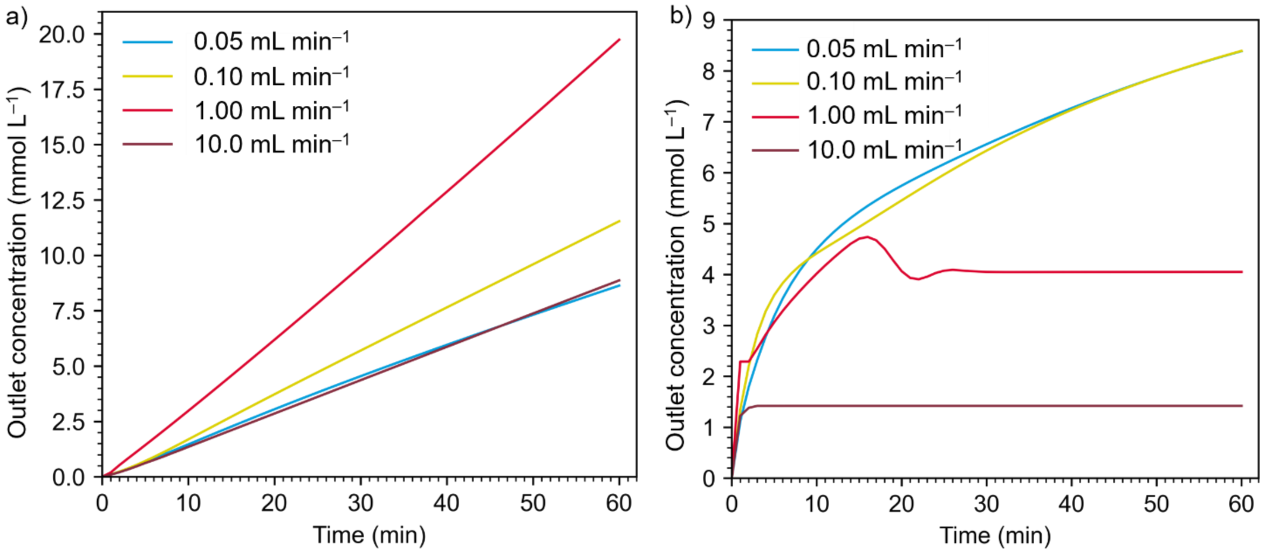

Figure S28 | a) Simulated outlet concentrations of epoxide from the upper (organic) compartment under counter-current flow operation mode and at different flow rates. b) Simulated outlet concentrations of glyceraldehyde from the lower (aqueous) compartment under co-current flow operation mode and at different flow rates. For each simulation, absolute flow rates were the same for both compartments.

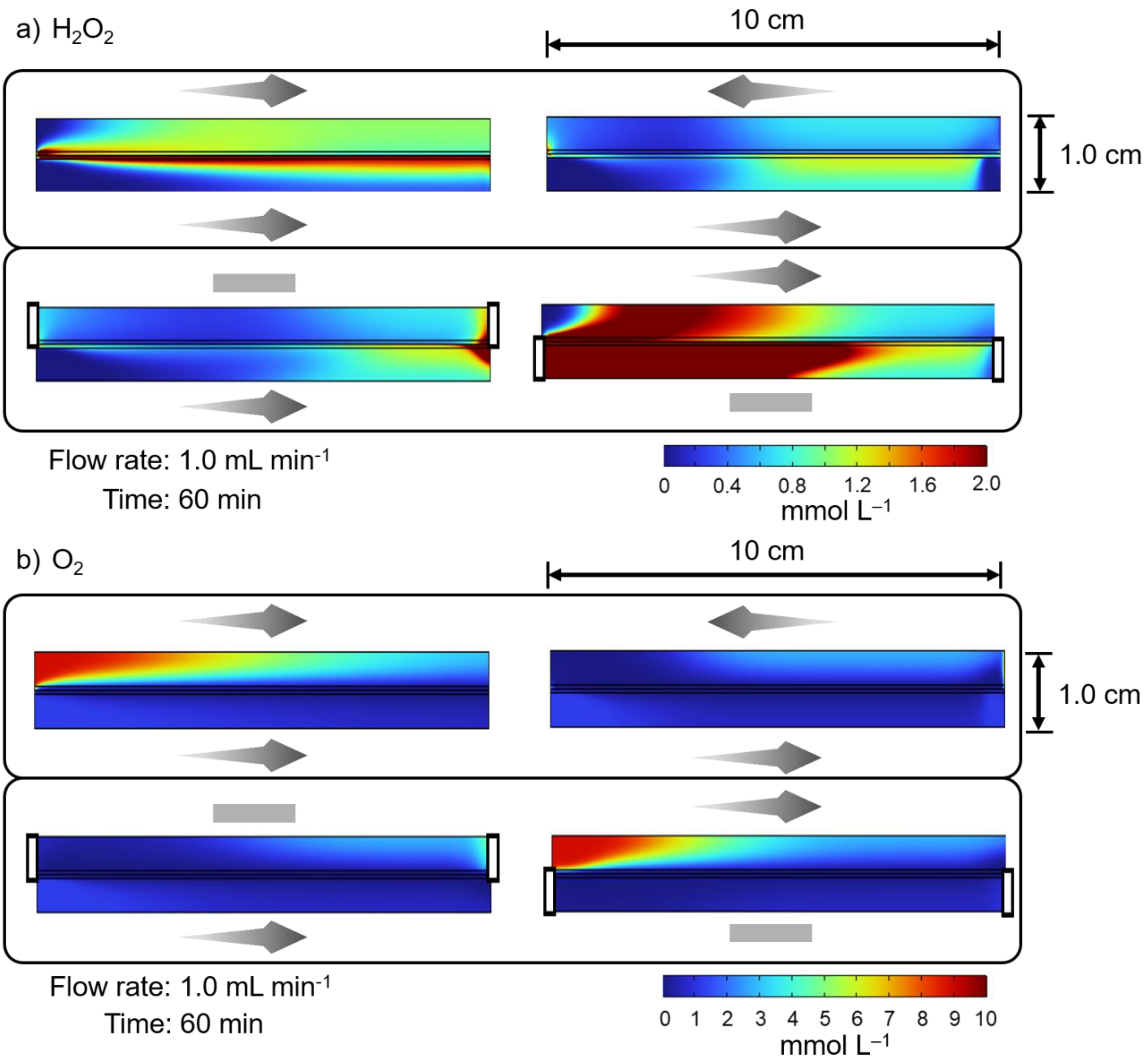

Figure S29 | Simulated concentration profiles of (a) H_2O_2 and (b) O_2 under different flow operation modes after 60 min reaction at 1.0 mmol L^{-1} flow rate. From left to right and top to bottom: co-current, counter-current, mono flow (aqueous), mono flow (organic). For dual flow simulations, absolute flow rates were the same for both compartments.

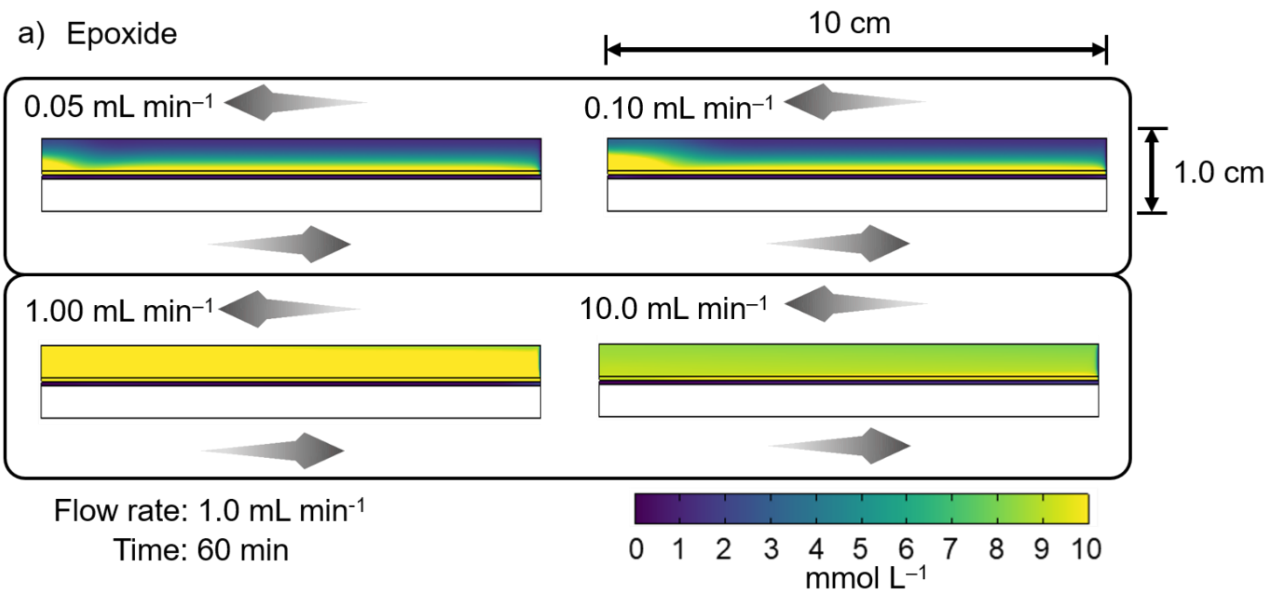

a) Epoxide

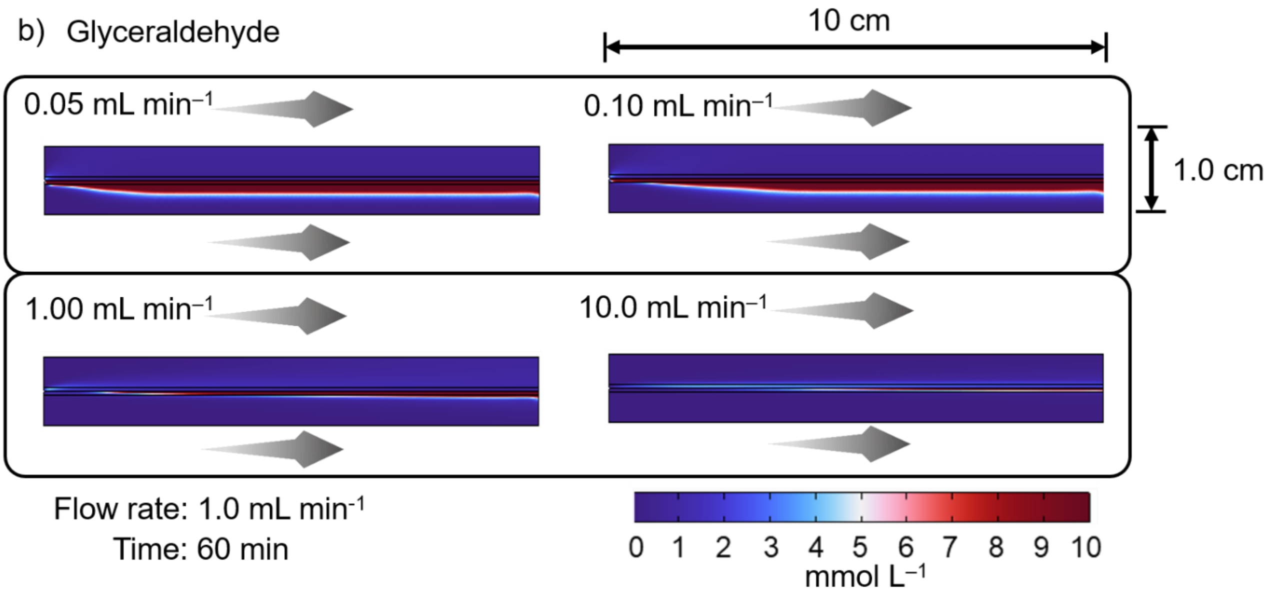

b) Glyceraldehyde

Figure S30 | Simulated concentration profiles of (a) epoxide under counter-current flow mode and (b) glyceraldehyde under co-current flow mode at different flow rates after 60 min. Absolute flow rates were the same for both compartments.

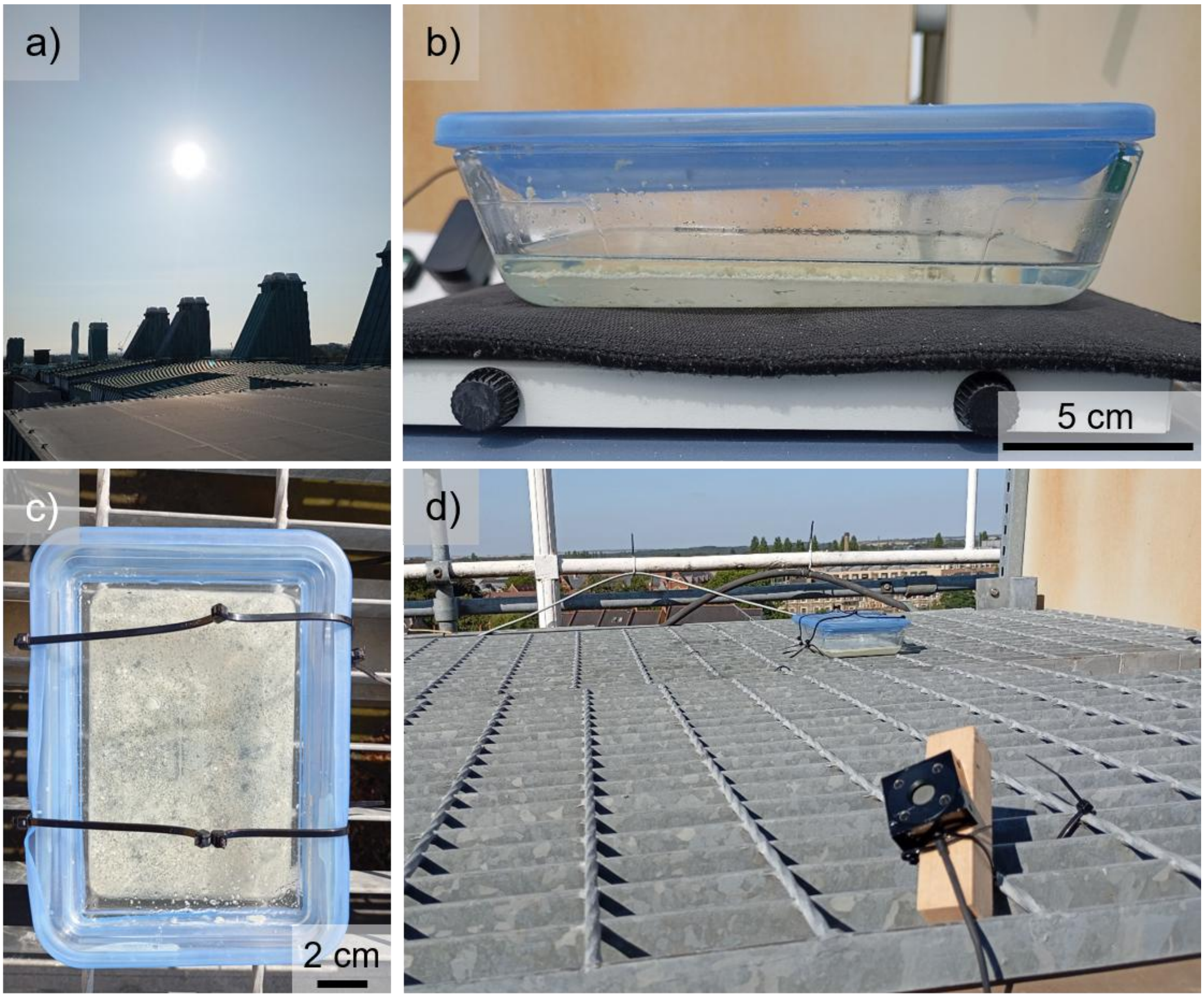

Figure S31 | Pictures of experimental setup for natural sunlight-driven photocatalysis. a) Sun on the rooftop of the Department of Chemistry at the University of Cambridge at 9 am on the 14th August 2025. b) Side and c) top view of the glass box photoreactor. d) Photodiode of the Newport 843-R light power meter recording the intensity of natural sunlight.

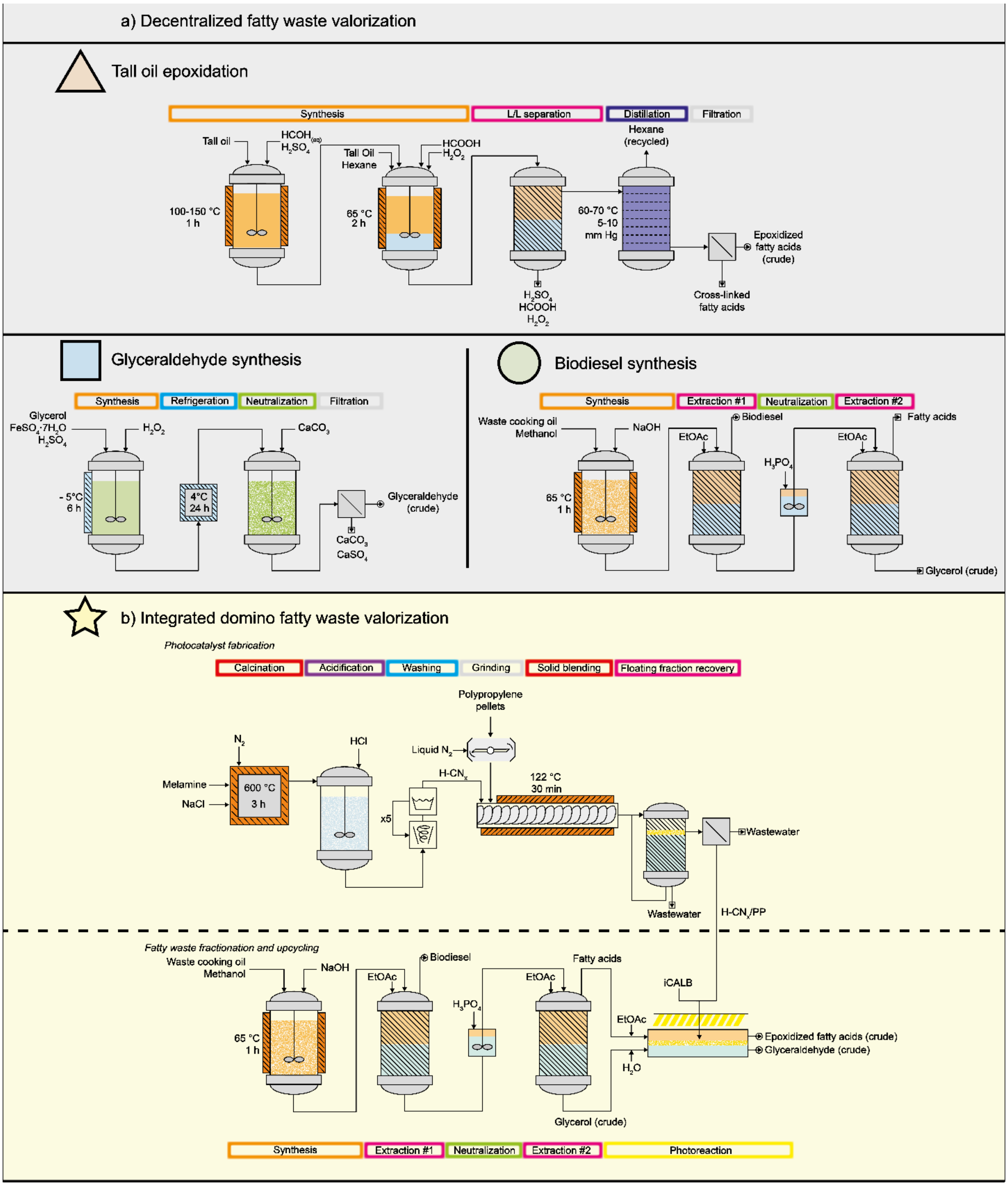

Figure S32 | Process diagrams evaluated for the cradle-to-gate life cycle assessment of (a) the decentralized valorization of fatty waste consisting of tall oil epoxidation,[28, 29] glyceraldehyde synthesis,[30] and biodiesel synthesis,[31] and (b) the integrated photocatalytic domino photocatalytic valorization of fatty waste producing biodiesel, epoxidized fatty acids and glyceraldehyde in the same plant.

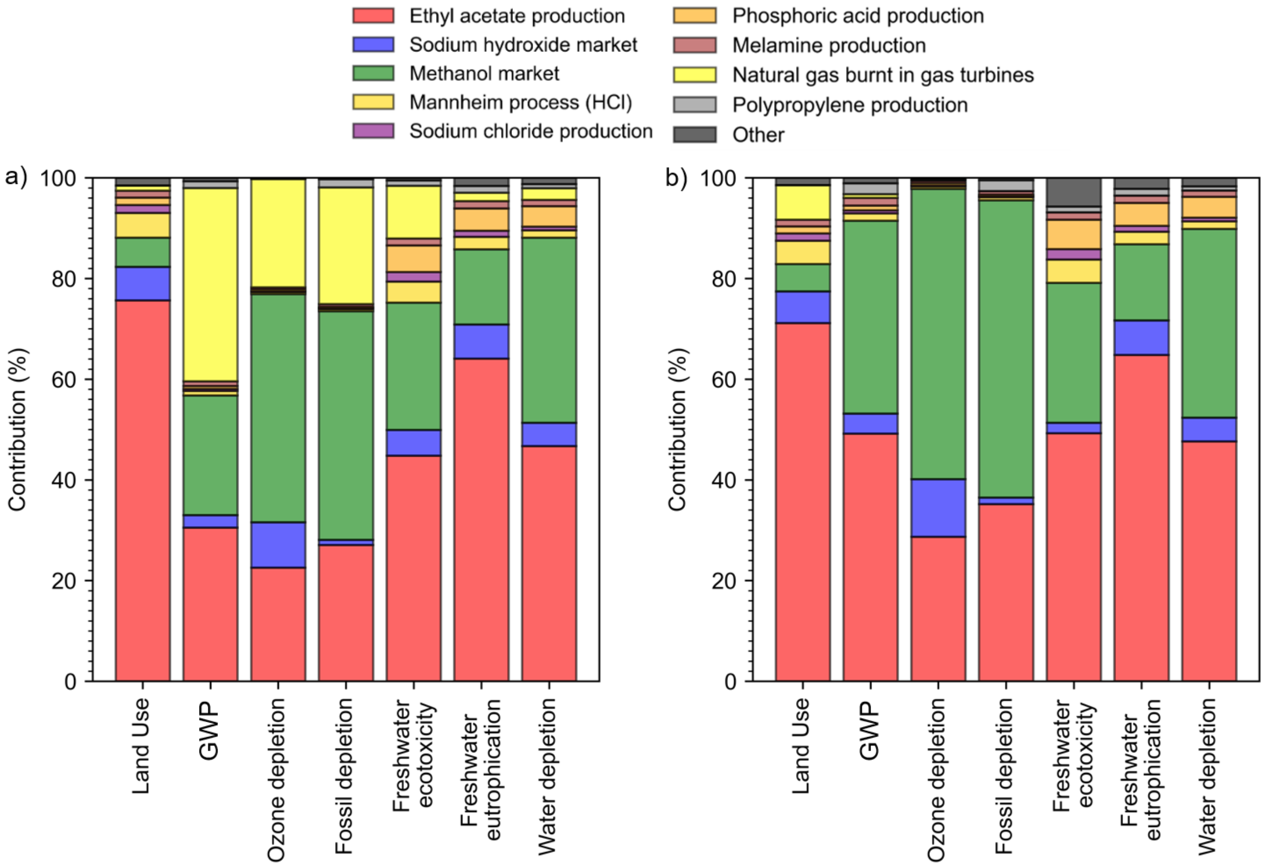

Figure S33 | Environmental impact hotspot analysis of integrated domino photocatalytic valorization of fatty waste with (a) fossil fuel and (b) renewables-derived energy sources.

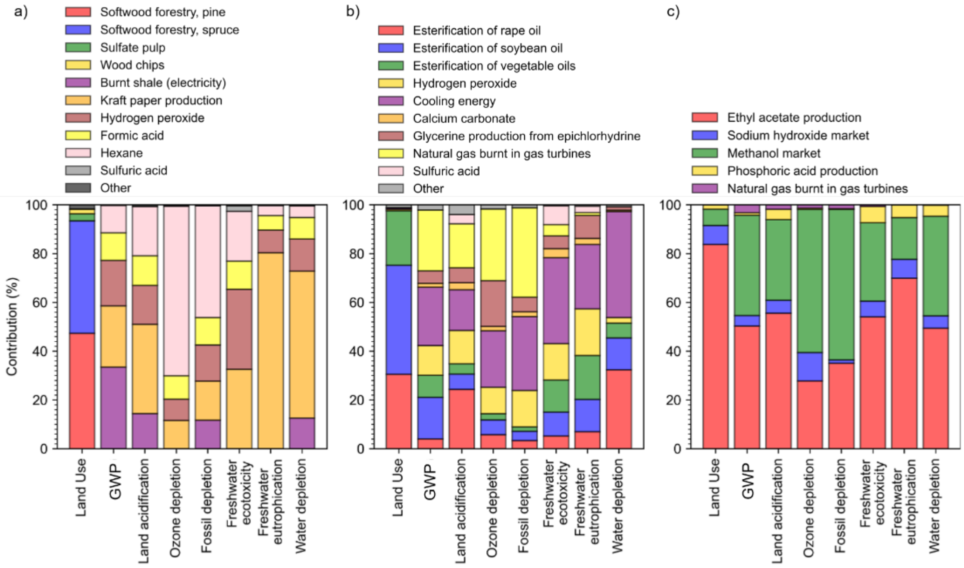

Figure S34 | Environmental impact hotspot analysis of the three individual processes for decentralized fatty waste valorization: a) tall oil epoxidation, b) glyceraldehyde synthesis, c) biodiesel synthesis.

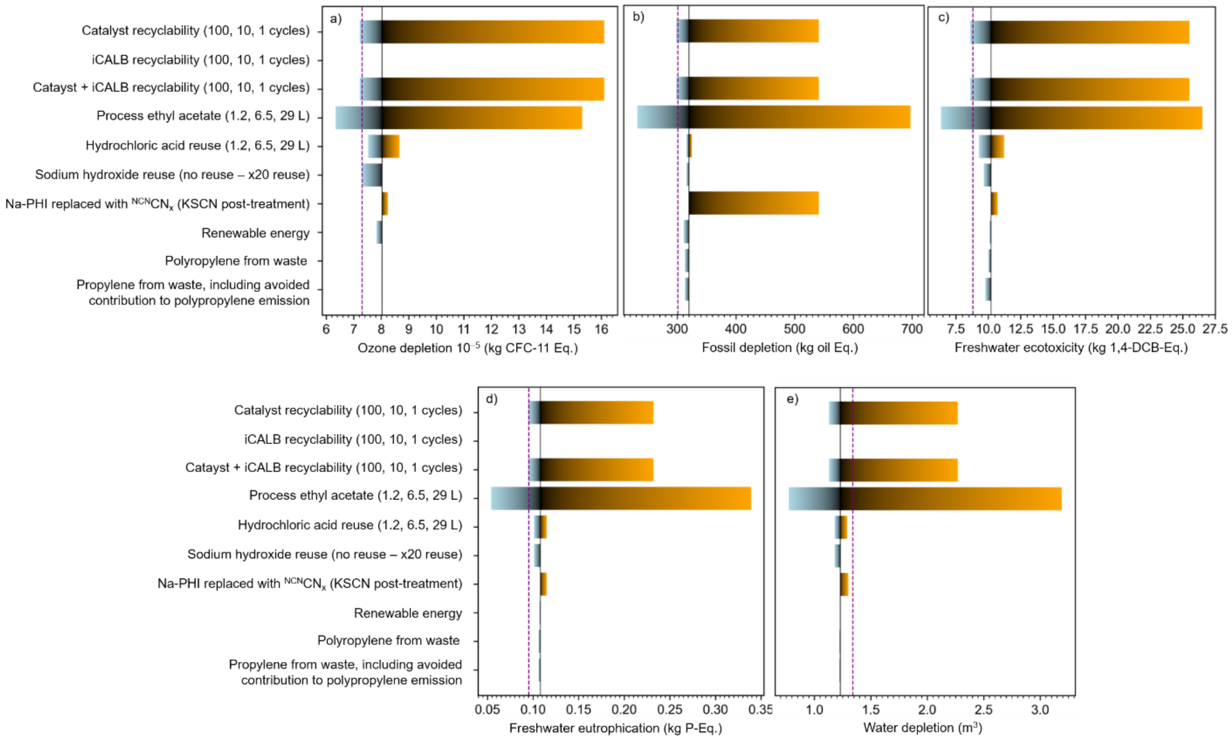

Figure S35 | Sensitivity analysis of integrated photocatalytic domino photocatalytic valorization of fatty waste on a) ozone depletion, b) fossil depletion, c) freshwater exotoxicity, d) freshwater eutrophication, and e) water depletion. The effects of continuous variables (above horizontal dotted line) and point variables (below horizontal dotted line) are shown. For continuous variables, values for optimistic, base, and pessimistic cases are reported in brackets on the left. The vertical purple dotted line indicates the total environmental impact of the decentralized fatty waste valorization (tall oil epoxidation + glyceraldehyde synthesis + biodiesel synthesis).

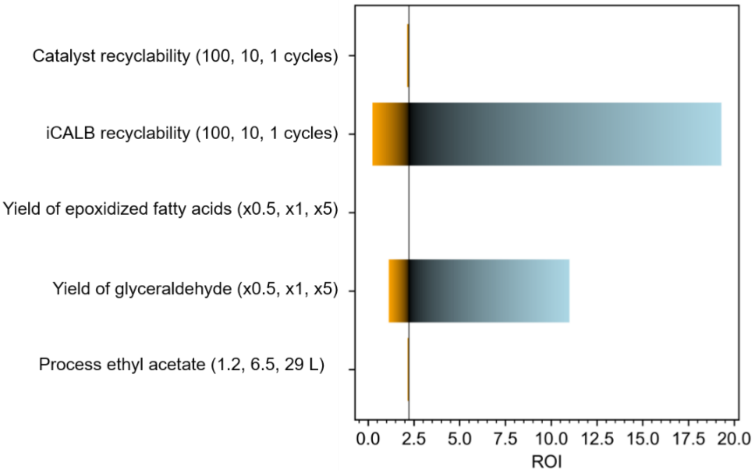

Figure S36 | Sensitivity analysis of integrated photocatalytic domino photocatalyitc valorization of fatty waste on relative ROI.

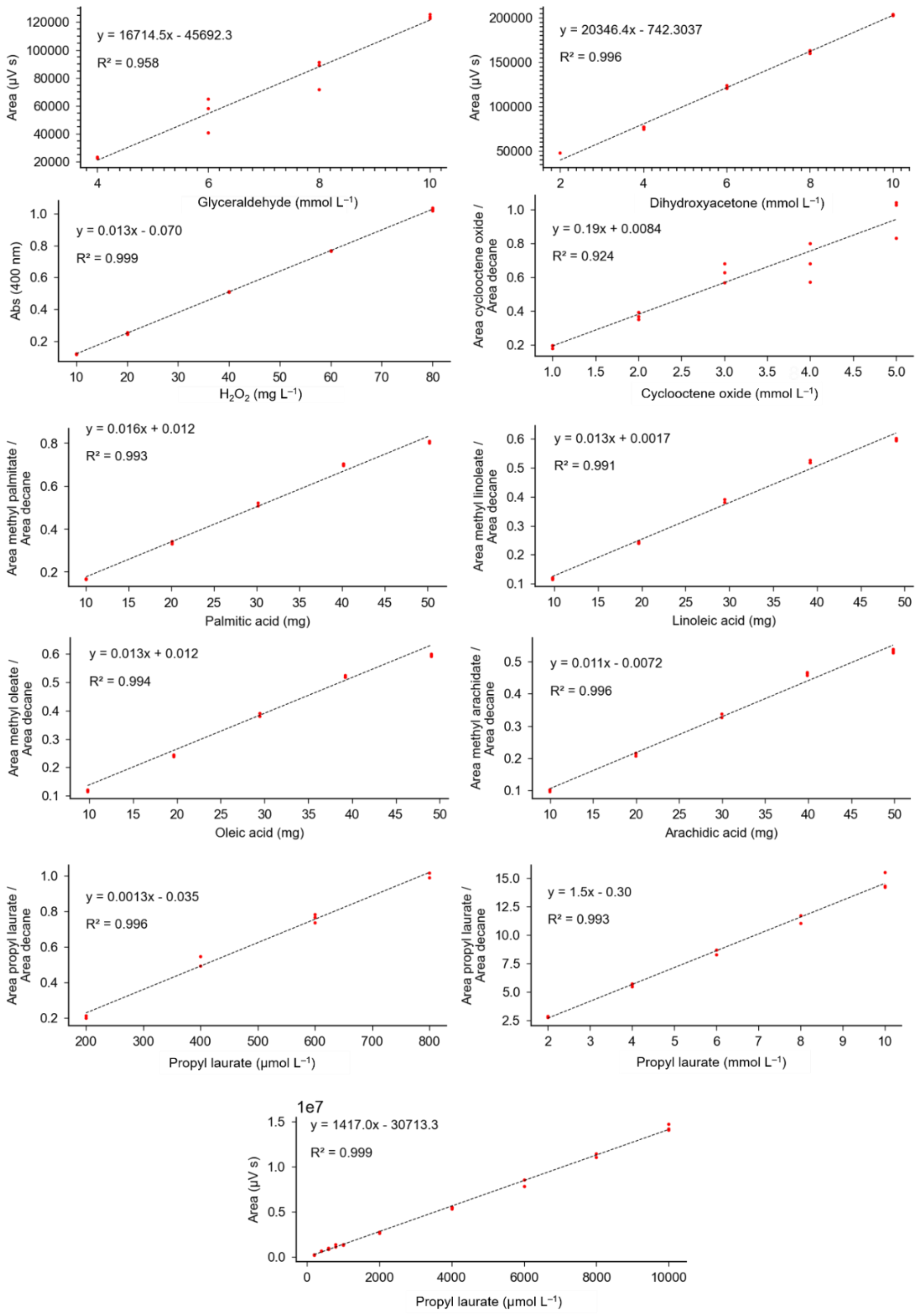

Figure S37 | Calibration curves of products quantified in this work. Red dots are data points (three for each standard concentration). Dotted lines are calibration curves obtained by linear fitting. Fitted curve equation and corresponding R^2 value are reported on each graph. For the determination of propyl laurate, two calibration curves with internal standards at different concentration ranges and one calibration curve with external standards were built.

Table S1 | Band position of the samples synthesized in this work

Sample	Bandgap (eV)	Valence band edge (eV)	Conduction band edge (eV)	Valence band edge (V vs SHE)	Conduction band edge (V vs SHE)
K-CN$_x$	2.65	6.98	4.33	2.54	-0.11
H-CN$_x$	2.87	6.93	4.06	2.47	-0.38

Table S2 | Recovered floating fraction and CN$_x$ content from the fabrication of CN$_x$/PP floatable composites

Composite[1]	Floating fraction (%)	CN$_x$ content (wt%)
H-CN$_x$/PP	37.3±3.2	37.1
K-CN$_x$/PP	26.7±4.3	25.3

[1] Samples were fabricated from 200 mg CN$_x$ and 133 mg PP.

Table S3 | ζ-Potential and pH generated in an aqueous suspension of carbon nitride (1 mg mL^{-1}).

Catalyst	ζ-Potential (mV)	pH
H-CN$_x$	-34.7±0.3	4.2
K-CN$_x$	-31.2±0.3	8.2

Table S4 | Comparison of ORR catalytic activity of H-CN_x and K-CN_x in acidified medium.

Catalyst	**Additive**	**H_2O_2 (mM)**
H-CN_x	None	14.3±1.2
K-CN_x	HCl[1]	16.4±1.2

[1] HCl 0.1 M was added to adjust the pH to ~4
Reaction conditions: catalyst (2.0 mg), 30 wt% aqueous glycerol (2 mL), O_2 (1 atm), 450 nm (40±4 mW cm^{-2}), 25 °C, 1 h.

Table S5 | Stoichiometry of ORR coupled with glycerol oxidation.

Product	**Concentration (mM)**
H_2O_2	26.0±10.8
Glyceraldehyde	29.5±4.6

Reaction conditions: H-CN_x/PP (20 mg), aqueous glycerol (30 wt%, 2 mL), 450 nm (40±4 mW cm^{-2}), O_2 (1 atm), 25 °C, 1 h.

Table S6 | Control experiments on photochemo-enzymatic epoxidation.[1]

Entry	Variation	Epoxide (mM)	H_2O_2 (mM)	Glyceraldehyde (mM)	Dihydroxyacetone (mM)
Substrate: cis-cyclooctene					
1	None	22.8±1.6	15.55±0.02	117.7±1.0	17.6±0.1
2	No H-CN_x/PP	0.4±0.2	N/D[2]	N/D[2]	N/D[2]
3	No iCALB	2.2±0.1	30.8±1.2	247.7±0.5	31.7±0.5
4	No irradiation	N/D[2]	N/D[2]	N/D[2]	N/D[2]
Substrate: oleic acid					
5	None	8.9±1.1	6.4±0.1	291±20	24.3±2.1
6	No glycerol[3]	3.0±0.8	8.2±0.3	/	/
7	No glycerol No ethyl acetate[3]	/	0.48±0.03	/	/
8	Free CALB (not immobilized)[4]	1.0±0.5	4.9±3.8	340±14	20.1±1.5
9	H-CN_x (not floatable)[5]	5.8±1.9	12.2±3.6	144±38	10.7±0.6
10	Free CALB and H-CN_x (not floatable)[4][5]	0.7±0.3	6.31±0.04	301.4±0.9	23.0±1.5

[1] Standard reaction conditions: H-CN_x (20 mg), iCALB (40 mg), aqueous glycerol (30 wt%) (2 mL), cis-cyclooctene in ethyl acetate (20 vol%, 2 mL) or oleic acid in ethyl acetate (40 wt%, 2 mL), 25 °C, 16 h.

[2] N/D: not detected.

[3] In the presence of ethyl acetate, H_2O_2 was produced from the oxidation of ethanol from iCALB-catalyzed ethyl acetate hydrolysis. Acetaldehyde was detected in the aqueous phase at a concentration of 7.3±0.2 mM in the absence of glycerol, comparable with the H_2O_2 produced. With 30 wt% glycerol, acetaldehyde concentration dropped to 0.77±0.14 mM, indicating that glycerol contributed the most as an electron donor.

[4] 40 mg of iCALB (5000 U g^{-1}) were replaced with 22 mg of Lipase B Candida antarctica, recombinant from *Aspergillus oryzae* (9000 U g^{-1}).

[5] 20 mg H-CN_x were replaced with 6 mg of H-CN_x in dispersion.

Table S7 | Control experiments on iCALB-catalyzed oleic acid epoxidation.[1]

Entry	Variation	Epoxide (mM)	H_2O_2 consumed (mM)
1	None[1]	18.5±2.8	21.9±0.6
2	+ octanoic acid[2]	22.3±0.5	28.4±7.2
3	No iCALB	2.8±2.7	4.9±4.9
4	48 h reaction time	18.9±0.3	37.5±0.5
5	20 mM H_2O_2 (1/2 of std conditions)	5.8±2.1	14.7±0.1

[1] Standard reaction conditions: iCALB (40 mg), aqueous H_2O_2 (40 mM) (2 mL), oleic acid in ethyl acetate (40 wt%, 2 mL), 25 °C, 16 h.

[2] 100 mM in 2 mL ethyl acetate

Table S8 | Activity of the integrated system over 6 days continuous operation.[1]

Time	Epoxide (mM)	H_2O_2 (mM)	Glyceraldehyde (mM)
3 days	38.7±5.0	7.38±1.39	113.6±4.1
6 days	62.7±4.7	1.19±0.50	213.5±10.6

[1] Reaction conditions: aqueous glycerol (30 wt%, 2 mL), oleic acid in ethyl acetate (40 wt%, 2 mL), H-CN_x/PP (20 mg), iCALB (40 mg), O_2 (1 atm), 450 nm (25 mW cm^{-2}), 25°C, 6 days. After 3 days, the liquid phases were replaced, and 40 mg iCALB were added.

Table S9 | Comparison of activity of H-CN_x/PP with different particle size in the integrated domino L|S|L photocatalysis.[1]

Particle size	Epoxide (mM)	H_2O_2 (mM)	Glyceraldehyde (mM)
0.5–1.0 cm (coarse, as fabricated)	1.49±0.15	10.7±1.2	36.4±4.9
0.1–0.5 cm (after cryogenic grinding)	0.39±0.06	2.6±0.7	14.6±3.4

[1] Reaction conditions: aqueous glycerol (30 wt%, 2 mL), oleic acid in ethyl acetate (40 wt%, 2 mL), H-CN_x/PP (20 mg), iCALB (40 mg), O_2 (1 atm), 450 nm (25 mW cm^{-2}), 25°C, 2h.

Table S10 | Results of accurate LC-MS analysis of epoxidized oleic acid.

Name	Molecular formula	Molecular mass (calc'd) (Da)	Molecular mass (found, [M-H$^+$]) (Da)[1]	Relative error (ppm)[1]	Detector counts[1]
Epoxystearic acid	$C_{18}H_{34}O_3$	298.25079	297.24333±0.00005	-0.5±0.2	52081±43823
Epoxystearic acid-[^{18}O]	$C_{18}H_{34}O_2[^{18}O]$	300.25504	299.24747±0.00005	-1.0±0.1	3849±131

[1] Errors calculated as the standard deviation from three injections

Table S11 | Composition of the biodiesel fraction extracted from vegetable oil samples.

FAME	Relative amount (wt%)[1]					
	Rapeseed	Sunflower	Olive	Soybean	Palm	Used vegetable oil
Palmitate (16:0)	5.5	7.2	18.3	13.9	48.0	9.5
Stearate (18:0)	0.0	2.2	2.3	4.6	0.7	3.6
Oleate (18:1, cis-Δ^9)	62.9	50.7	42.4	37.5	26.2	35.2
Linoleate (18:2, cis,cis-Δ^9 Δ^{11})	29.9	39.6	36.3	43.5	26.2	50.9
Arachidate (20:0)	0.5	0.2	0.3	0.3	0.4	0.3
Gondolate (20:1, cis-Δ^{11})	1.2	0.1	0.3	0.2	0.2	0.5

[1] Estimated from the ratio of the areas in the TCD (thermal conductivity detector) gas-chromatogram

Table S12 | Recovered glycerol, fatty acids, biodiesel, and soap fractions from used vegetable oil.

Vegetable oil	Starting mass (g)	Methanol mass (g)	Recovered fraction (wt%)			
			Glycerol	Fatty acids	Biodiesel	Soap
Used vegetable oil	35.2	7.5	3.3	2.3	66.2	6.3

Table S13 | Kinetic parameters defined in finite element simulation studies.

Parameter	Value (min^{-1})	Ref
k_1	6.21	6
k_2	0.0262	6
k_3	0.30	20

Table S14 | Partition and diffusion coefficients defined in finite element simulation studies. References are indicated next to values in the table where relevant.

Species	**Partition coefficient ethyl acetate/water**	**Diffusion coefficient water (10^{-9} m^2 s^{-1})**	**Diffusion coefficient ethyl acetate (10^{-9} m^2 s^{-1})**
H_2O_2	0.17[36]	1.60[22]	10.0[23]
O_2	7.30[1]	2.20[37]	3.46[38]
Epoxide	1000[2]	/	1.0[3]
Glyceraldehyde	450[39]	0.25[24]	3.2[40]

[1] Calculated as the ratio between O_2 solubilities in water (1.22 mmol L^{-1}) and ethyl acetate (8.91 mmol L^{-1})[21]

[2] Virtually infinite value to constrain the epoxide in the organic phase.

[3] Approximate representative value. No reliable references available.

Table S15 | Life cycle inventory for integrated domino photocatalytic valorization of fatty waste. Providers for each flow are the corresponding market global production, unless otherwise specified.

Integrated photocatalytic domino valorization of fatty waste				
Category	**Inventory**	**Quantity**	**Unity**	**Notes**
Output	Epoxidized fatty acids	1	kg	
	Glyceraldehyde	1.52	kg	
	Biodiesel	62.9	kg	
Input	*Catalyst synthesis and fabrication*			
	Melamine	0.867	kg	Assuming 60% yield of Na-PHI from a 1:10 w/w mixture of melamine and sodium chloride, 100% yield of H-PHI from Na-PHI, and a floating fraction of 37% from a 6:4 w/w mixture of H-PHI and polypropylene
	Sodium chloride	8.67	kg	
	Hydrochloric acid (37%)	51.3	L	
	Polypropylene	3.52	kg	
	Liquid nitrogen	11.4	L	
	Immobilized enzyme			
	iCALB	2.29	kg	See Table S17
	Fatty acid fractionation			
	Waste cooking oil	1144	kg	
	Sodium hydroxide	12.4	kg	
	Methanol	280	L	
	Phosphoric acid$_{(aq)}$ (85%)	1.72	L	
	Process flows			
	Ethyl acetate, process	72.1	L	
	Water, process	50000	L	
	Oxygen	20	L	
	Electricity			Modelled as natural gas burned in turbine or from renewable energy
	Annealing (catalyst)	30.8	kWh	Assuming an industrial furnace operating at 550°C for 3h. Electricity consumed for centrifugation and grinding is negligible
	Heating (biodiesel synthesis)	1.5	kWh	Estimated to reflux methanol for 1h
Emission[1]	Wastewater	50000	L	Emitted to fresh water
	Ammonia	1.12	kg	Emitted to air. Assuming two moles of ammonia released per mole of melamine used for catalyst syntesis[41]

[1] NaOH is assumed to be neutralized with excess HCl. Ethyl acetate is assumed to be recycled by evaporation.

Table S16 | Life cycle inventory for tall oil epoxidation.[28, 29] Providers for each flow are the corresponding market global production, unless otherwise specified.

Tall oil epoxidation				
Category	**Inventory**	**Quantity**	**Unity**	**Notes**
Output	Epoxidized tall oil	1	kg	Tall oil is approximated as a mixture of 50 wt% linoleic acid and 40 wt% oleic acid. A 99% epoxidation yield was assumed
Input	Tall oil	1.06	kg	Provided from kraft paper production
	Formaldehyde$_{(aq)}$ (37%)	0.0106	kg	
	Sulfuric acid	0.0106	kg	
	Hexane	1.01	L	
	Formic acid$_{(aq)}$ (91%)	0.137	kg	
	Hydrogen peroxide$_{(aq)}$ (50%)	0.41	kg	
	Water, process	3640	L	For distillation and reflux, assuming 0.5 L min^{-1} flow rate for both processes. Water used for washing in separatory step is negligible.
	Electricity			Modelled as natural gas burned in turbine or from renewable energy
	Heating	0.72	kWh	Heating for distillation, assuming a 1 kW mantel.
	Stirring	0.12	kWh	
Emission	Sulfuric acid	0.0106	kg	Emitted to fresh water
	Formic acid$_{(aq)}$ (91%)	0.137	kg	Emitted to fresh water
	Hydrogen peroxide$_{(aq)}$ (50%)	0.0326	kg	Emitted to fresh water
	Cross-linked fatty acid	0.0495	kg	Modelled as "plastic waste" emission
	Water from reaction	0.313	kg	Emitted to fresh water
	Wastewater	3640	L	Emitted to fresh water

Table S17 | Life cycle inventory for glyceraldehyde production.[30] Providers for each flow are the corresponding market global production, unless otherwise specified.

Glyceraldehyde synthesis				
Category	**Inventory**	**Quantity**	**Unity**	**Notes**
Output	Glyceraldehyde	1.52	kg	
Input	Glycerol	1.81	kg	
	Iron(II) sulfate heptahydrate	0.151	kg	
	Hydrogen peroxide$_{(aq)}$ (6%)	12.1	L	
	Sulfuric acid	0.151	L	
	Calcium carbonate	0.756	kg	
	Process flows			
	Water, process	9.83	L	
	Electricity			Modelled as natural gas burned in turbine or from renewable energy
	Cooling energy	17.5	kWh	Estimated as the energy needed to bring the aqueous reacting solution to 5°C, leave it at temperature for 6 h, and then store in a refrigerator for 24h
	Filtration	0.0250	kWh	Estimated as 1 kWh m^{-3} [42]
	Ice fabrication	60.5	kWh	Estimated from the energy needed to solidify 300 g of water from room temperature
Emission	Iron(II) sulfate heptahydrate	00.151	kg	
	Calcium carbonate	0.756	kg	Emitted to ground water
	Calcium sulfate	0.302	kg	Modelled within the market for waste gypsum
	Wastewater	9.83	L	Emitted to fresh water

Table S18 | Life cycle inventory for biodiesel synthesis.[43] Providers for each flow are the corresponding market global production, unless otherwise specified.

Biodiesel synthesis				
Category	**Inventory**	**Quantity**	**Unity**	**Notes**
Output	Biodiesel	62,9	kg	
Input	Waste cooking oil	1.14	kg	
	Sodium hydroxide	1.24	kg	
	Methanol	22.0	kg	
	Phosphoric acid$_{(aq)}$ (85%)	0.172	L	
	Process flows			
	Ethyl acetate, process	7.21	L	
	Water, process	5000	L	
	Electricity			Modelled as natural gas burned in turbine or from renewable energy
	Heating	1.50	kWh	Estimated energy needed to reflux methanol for 1h
Emission	Wastewater	5000	L	Emitted to fresh water

Table S19 | Life cycle inventory for iCALB fabrication.[1]

Category	**Inventory**	**Quantity**	**Unity**	**Notes**
Output	iCALB	1	kg	
Input	Energy	121	MJ	
Emission	CO_2	16.3	kg	Emitted to air
	Ethylene	0,00732	kg	Emitted to air
	Phosphate	0,013	kg	Emitted to freshwater
	Sulfur dioxide	0,133	kg	Emitted to air

[1] The impact was assessed as the average from reported values for immobilized carbamoylase and hydantoinase.[32] Immobilization has the highest environmental impact, over culture preparation and purification. The impact of immobilization may be overestimated, as the reported enzymes are grafted on the specialty polymer glycidyl methacrylate, while iCALB is immobilized on widely available poly(methyl methacrylate) cross-linked with divinylbenzene.[44]

Table S20 | Scoring rubric for the pedigree approach for estimating uncertainty.[33, 34] The sum of these scores were then assigned a geometric standard deviation as detailed in Supplementary Note 6 and Tables S19-20.

Category	**Score**				
	1	**2**	**3**	**4**	**5**
Reliability	Verified data based on measurements	Verified data partly based on assumptions of non-verified data based on measurements	Non-verified data partly based on qualified estimates	Qualified estimate (by industrial expert)	Non-qualified estimate
Completeness	Representative data from all sites relevant for the market considered over an adequate period to even out normal fluctuations	Representative data from >50% of the sites relevant for the market considered over an adequate period to even out normal fluctuations	Representative data from only some sites (<<50%) relevant for the market considered OR >50% of sites but from shorter periods	Representative data from only one site relevant for the market considered OR some sites but from shorter periods	Representativeness unknown or data from a small number of sites AND from shorter periods
Temporal correlation	Less than 3 years of difference to our reference year	Less than 6 years of difference to our reference year	Less than 10 years of difference to our reference year	Less than 15 years of difference to our reference year	Age of data unknown or more than 15 years of difference to our reference year
Geographical correlation	Data from area under study	Average data from larger area than area under study, or from similar area	Data from smaller area than area under study, or from similar area	Data from area with slightly similar production conditions	Data from unknown OR distinctly different area
Further technological correlation	Data from enterprises, processes and materials under study (identical technology)	Data from processes and materials under study but from different enterprises	Data on related processes or materials but same technology, OR data from processes and materials under study but from different technology	Data on related processes or materials but different technology, OR data on laboratory scale processes and same technology	Data on related processes or materials but on laboratory scale of different technology

Table S21 | Pedigree matrix to determine uncertainty factors as geometric standard deviations.[33]

Score indicator	1	2	3	4	5
Reliability	1	1.05	1.1	1.2	1.5
Completeness	1	1.02	1.05	1.1	1.2
Temporal correlation	1	1.03	1.1	1.2	1.5
Geographical correlation	1	1.01	1.02		1.1
Further technological correlation	1		1.2	1.5	2
Sample size	1	1.02	1.05	1.1	1.2

Table S22 | Uncertainty scores and geometric standard deviations assigned to different components of the life cycle inventories of all the evaluated processes. Uncertainty factors were determined as the unweighted average of the uncertainty factors determined for each score indicator from Tables S18-19.

Category	**Inventory**	**Score**						**Uncertainty factor (from Table S19)**
		Reliability	Completeness	Temporal correlation	Geographical correlation	Further technological correlation	Total	
Tall oil epoxidation								
Inputs	Tall oil	2	4	5	3	2	16	1,174
	Formaldehyde$_{(aq)}$ (37%)	2	4	5	3	2	16	1,174
	Sulfuric acid	2	4	5	3	2	16	1,174
	Hexane	2	4	5	3	2	16	1,174
	Formic acid$_{(aq)}$ (91%)	2	4	5	3	2	16	1,174
	Hydrogen peroxide$_{(aq)}$ 50%	2	4	5	3	2	16	1,174
	Water, process	3	4	5	3	3	18	1,174
	Electricity	3	4	5	3	3	18	1,184
Emissions	Sulfuric acid	3	4	5	3	3	18	1,184
	Cross-linked fatty acid	3	4	5	3	3	18	1,184
	Formic acid	3	4	5	3	3	18	1,184
	Water from reaction	3	4	5	3	3	18	1,184
	Wastewater	3	4	5	3	3	18	1,184
	Hydrogen peroxide$_{(aq)}$ (50%)	3	4	5	3	3	18	1,184
Glyceraldehyde synthesis								
Input	Glycerol	2	4	1	3	4	14	1,134
	Iron (II) sulfate heptahydrate	2	4	1	3	4	14	1,134
	Hydrogen peroxide$_{(aq)}$ (6%)	2	4	1	3	4	14	1,134
	Sulfuric acid	2	4	1	3	4	14	1,134
	Water	3	4	1	3	4	15	1,134
	Calcium carbonate	2	4	1	3	4	14	1,134
	Electricity	3	4	1	3	4	15	1,144
Emission	Calcium carbonate	3	4	1	3	4	15	1,144
	Calcium sulphate	3	4	1	3	4	15	1,144
	Iron (II) sulfate heptahydrate	3	4	1	3	4	15	1,144
Integrated domino photocatalytic valorization of fatty waste (including biodiesel synthesis)								
Input	*Catalyst synthesis and fabrication*							
	Melamine	1	4	1	3	4	13	1,124
	Sodium chloride	1	4	1	3	4	13	1,124
	Hydrochloric acid$_{(aq)}$ (37%)	1	4	1	3	4	13	1,124
	Polypropylene	1	4	1	3	4	13	1,124
	Liquid nitrogen	1	4	1	3	4	13	1,124

	Immobilized enzyme							1,124
	iCALB	1	4	1	3	4	13	1,124
	Fatty acid fractionation							
	Waste cooking oil	1	4	1	3	4	13	1,124
	Sodium hydroxide	1	4	1	3	4	13	1,124
	Methanol	1	4	1	3	4	13	1,124
	Phosphoric acid$_{(aq)}$ (85%)	1	4	1	3	4	13	1,124
	Process flows							
	Ethyl acetate, process	1	4	1	3	4	13	1,134
	Water, process	2	4	1	3	4	14	1,134
	Oxygen	2	4	1	3	4	14	1,134
	Electricity	2	4	1	3	4	14	1,134
Emission	Wastewater	2	4	1	3	4	14	1,134
	Ammonia	3	4	5	3	4	19	1,234

Table S23 | Environmental impact analysis results for individual processes of decentralized fatty waste valorization (tall oil epoxidation, glyceraldehyde synthesis, biodiesel synthesis), their total for decentralized fatty waste valorization, and for integrated domino photocatalytic fatty waste valorization. The cumulative energy distribution computation tool does not have uncertainty capabilities.

Category	**Unit**	**Tall Oil Production**	**Glyceraldehyde synthesis**	**Biodiesel synthesis**	**Decentralized fatty waste valorization**	**Integrated fatty waste valorization**
100 g epoxidized tall oil, 152 g glyceraldehyde, 6.29 kg biodiesel						
Land Use	m^{2}a	0.64±0.23	0.76±0.10	1.0±0.2	2.4±0.3	1.2±0.3
GWP	kg CO_2-Eq	0.32±0.025	1.7±0.2	33±2.7	35.0±2.7	64±4.6
Land Acidification	kg SO_2-Eq	1.3±0.12E-3	5.5±0.6E-3	0.14±0.02	0.15±0.02	2.7±0.5
Ozone depletion	kg CFC-11-Eq	4.7±2.0E-8	1.4±0.4E-8	6.7±1.2E-6	6.8±1.2E-6	1.1±0.4E-5
Fossil depletion	kg oil-Eq	0.14±0.01	0.49±0.05	29±2.3	29.6±2.3	46±3.4
Freshwater ecotoxicity	kg 1,4-DCB-Eq	5.7±1.5E-3	0.044±0.009	0.84±0.22	0.89±0.22	1.2±0.4
Freshwater eutrophication	kg P-Eq	1.7±0.8E-4	2.8±0.7E-4	9.2±3.2E-3	9.7±3.2E-3	11±4.6E-3
Water depletion	m^3	0.0012±0.0001	0.024±0.002	0.11±0.01	0.13±0.01	0.14±0.01
Energy	MJ	11	29	1278	1318	1729
1 kg epoxidized tall oil, 1.52 kg glyceraldehyde, 62.9 kg biodiesel						
Land Use	m^{2}a	6.4±2.3	7.6±1.0	10±2	24±3	12±2
GWP	kg CO_2-Eq	3.2±0.25	17±1.6	3.3±0.27E2	3.5±0.27E2	4.0±0.3E2
Land Acidification	kg SO_2-Eq	0.013±0.0012	0.055±0.006	1.4±0.2	1.5±0.2	27±5
Ozone depletion	kg CFC-11-Eq	4.7±2.0E-7	1.4±0.4E-7	6.7±1.2E-5	6.8±1.2E-5	7.9±1.8E-5
Fossil depletion	kg oil-Eq	1.4±0.1	49±5	2.9±0.23E2	3.0±2.3E2	3.2±0.3E2

Freshwater ecotoxicity	kg 1,4-DCB-Eq	0.057±0.015	0.44±0.09	8.4±2.2	8.9±2.2	10±3
Freshwater eutrophication	kg P-Eq	1.7±0.8E-3	2.8±0.7E-3	0.092±0.032	0.097±0.032	0.11±0.07
Water depletion	m^3	0.012±0.001	0.24±0.02	1.1±0.1	1.3±0.1	1.2±0.1
Energy	MJ	106	294	12780	13180	14073
1 kg epoxidized tall oil, 1.52 kg glyceraldehyde, 62.9 kg biodiesel + renewable nergy						
Land Use	m^{2}a	6.9±2.3	7.6±1.0	10±2	24±3	12±3
GWP	kg CO_2-Eq	2.1±0.2	13±1.3	3.3±0.26E2	3.5±0.27E2	3.7±0.3E2
Land Acidification	kg SO_2-Eq	0.011±0.001	0.045±0.004	1.4±0.2	1.5±0.2	26±5
Ozone depletion	kg CFC-11-Eq	4.7±1.7E-7	9.5±2.1E-7	7.1±1.6E-5	6.8±1.2E-5	7.9±1.7E-5
Fossil depletion	kg oil-Eq	1.2±0.1	3.2±0.5	2.9±0.27E2	3.0±2.3E2	3.1±0.3E2
Freshwater ecotoxicity	kg 1,4-DCB-Eq	0.059±0.014	0.44±0.08	8.1±1.6	8.9±2.2	9.8±2
Freshwater eutrophication	kg P-Eq	1.6±0.9E-3	2.9±0.8E-3	0.091±0.033	0.097±0.032	0.11±0.05
Eater depletion	m^3	0.010±0.001	0.24±0.03	1.1±0.1	1.3±0.1	1.2±0.1
Energy	MJ	99	217	12590	12906.7	13958

Table S24 | Continuous and point variations considered for uncertainty analysis studies, corresponding numerical cases and justifications for the proposed values.

Continuous variations				
Parameter	**Case**			**Justification**
	Pessimistic	Base	Optimistic	
Photocatalyst (H-CN$_x$/PP) recyclability	1 cycle	10 cycles	100 cycles	10 cycles demonstrated in this work. 100 cycles achievable with strategies to prevent composite swelling and catalyst leaching
iCALB recyclability	1 cycle	10 cycles	100 cycles	10 cycles demonstrated in this work. 100 cycles achievable with modification of the commercial resin with protective layers or stronger enzyme anchoring strategies
Joint H-CN$_x$/PP and iCALB recyclability	1 cycle	10 cycles	100 cycles	As above
Process ethyl acetate for washing	29 L	6.5 L	1.2 L	Optimistic: none or minimal washing, ethyl acetate only used for the dilution of fatty acids in the reacting organic phase. Base: 6x10 mL washing steps. Pessimistic: 6x20 mL washing steps
Hydrochloric acid (30 wt%) reuse	3.6 kg	18.1 kg	36.28 kg	Optimistic: 2 mL of HCl g^{-1} of catalyst. Base: 10 mL HCl g^{-1}catalyst. Pessimistic: 20 mL HCl g^{-1} catalyst.
Sodium hydroxide reuse		No reuse	20 reuses	Optimistic: assuming minimal consumption of NaOH in catalytic biodiesel synthesis, if recovered before dilution of glycerol with water to prevent residual triglycerides saponification. Base: discarded immediately after biodiesel synthesis.
Yield of epoxide (yield of glyceraldehyde scaled proportionally)	10 g	100 g	500 g	100 g extrapolated from the results of this work. 500 g achievable with reactor design to overcome mass transfer limitations (e.g. microfluidic reaction channels)
Point variations				
Catalyst variation: sodium poly(heptazine imides) (Na-PHI) replaced with cyanamide functionalized carbon nitride (^{NCN}CN$_x$)				
Energy from renewables				
Polypropylene from waste				
Polypropylene from waste, including avoided impact of polypropylene emission				

Table S25 | Sensitivity analysis results for selected parameters and cases for integrated domino photocatalytic valorization of fatty waste.

Continous variations								
Parameter	*Integrated domino photocatalytic valorization of fatty waste Pessimistic - Base - Optimistic*							
	Land use (m^2a)	GWP (kg CO_2-Eq.)	Ozone depletion (kg CFC-11-Eq.)	Fossil depletion (kg oil-Eq.)	Freshwater ecotoxicity (kg 1,4-DCB-Eq.)	Freshwater eutrophication (kg P-Eq.)	Water depletion (m^3)	Energy (MJ)
Photocatalyst (H-CN_x/PP) recyclability	24.3 - 11.9 - 10.6	913 - 392 - 340	16.1 - 8.03 - 7.22 E-5	541 - 320 - 298	25.5 - 10.2 - 8.6	0.232 - 0.108 - 0.095	2.27 - 1.23 - 1.13	2.42 - 1.42 - 1.32 E4
iCALB recyclability	11.9 - 11.9 - 11.9	392 - 392 - 392	8.03 - 8.03 - 8.03 E-5	320 -320 - 320	10.2 -10.2 -10.2	0.108 - 0.108 - 0.108	1.23 -1.23 - 1.23	1.69 - 1.42 - 1.40 E4
Joint H-CN_x/PP and iCALB recyclability	24.3 - 11.9 - 10.6	913 - 392 - 340	16.1 - 8.03 - 7.22 E-5	541 - 320 - 298	25.5 - 10.2 - 8.6	0.232 - 0.108 - 0.095	2.27 - 1.23 - 1.13	2.42 - 1.42 - 1.32 E4
Process ethyl acetate for washing	42.7 - 11.9 - 4.7	1011 - 392 - 248	15.3 - 8.03 - 6.34 E-5	697 - 320 - 232	26.5 - 10.2 - 6.35	0.339 - 0.108 - 0.054	3.19 - 1.23 - 0.773	3.10 - 1.42 - 1.03 E4
Hydrochloric acid (30 wt%) reuse	12.7 -11.9 - 11.2	408 - 392 - 380	8.66 - 8.03 - 7.52 E-5	325 - 320 - 316	11.2 - 10.2 - 9.28	0.115 -0.108 - 0.101	1.29 - 1.23 - 1.18	1.45 - 1.42 - 1.42 E4
Sodium hydroxide reuse	/ - 11.9 -11.1	/ - 392 - 379	/ - 8.03 - 7.29 E-5	/ - 320 - 316	/ - 10.2 - 9.64	/ - 0.108 - 0.101	/ - 1.23 - 1.18	/ - 1.42 - 1.40
Point variations								
Catalyst variation: sodium poly(heptazine imides) (Na-PHI) replaced with cyanamide functionalized carbon nitride ($^{NCN}CN_x$)	12.6 - 11.9 - /	423 - 392 - /	8.24 - 8.03 - / E-5	541 - 320 - /	10.7 - 10.2 - /	0.115 - 0.108 - /	1.30 - 1.23 - /	1.48 - 1.42 - / E4
Energy from renewables	/ - 11.9 - 11.9	/ - 392 - 370	/ - 8.03 - 7.83 E-5	/ - 320 - 311	/ - 10.2 - 10.1	/ - 0.108 - 0.107	/ - 1.23 - 1.23	/ - 1.42 - 1.40 E4
Polypropylene from waste streams	/ - 11.9 -11.8	/ - 392 -385	/ - 8.03 - 8.01 E-5	/ - 320 - 313	/ - 10.2 - 10.0	/ - 0.108 - 0.106	/ - 1.23 - 1.22	/ - 1.42 - 1.40 E4
Polypropylene from waste, including avoided impact of polypropylene emission	/ - 11.9 - 11.8	/ - 392 -378	/ - 8.03 - 8.01 E-5	/ - 320 - 313	/ - 10.2 - 9.77	/ - 0.108 - 0.106	/ - 1.23 - 1.22	/ - 1.42 - 1.40 E4

Decentralized valorization of fatty waste

	Pessimistic - Base - Optimistic							
Yield of epoxide (yield of glyceraldehyde scaled proportionally)	124 - 24.8 - 2.48	1790 - 358 - 35.8	36.5 - 7.30 - 0.730 E-5	1505 - 301 - 30.1	44.0 - 8.79 - 0.879	0.476 - 0.0952 - 0.00952	6.7 - 1.34 - 0.134	6.60 - 1.32 - 0.132 E4

Table S26 | Unity prices and revenues of individual components considered for the simplified relative techno-economic analysis of integrated domino photocatalytic valorization of fatty waste.

Consumables	**Price ($\$\,\mathrm{kg}^{-1}$)**	**Ref**
Hydrochloric acid$_{(aq)}$ (37%)	0.15	45, 46
Melamine	1.6	47
Sodium chloride	2.7	48
Liquid nitrogen	0.88	49, 50
Polypropylene	-0.037	51
iCALB	3134	52, 53
Ethyl acetate	1.12	54-56
Operational costs	**Price ($\$\,\mathrm{kWh}^{-1}$)**	**Ref**
Electricity	0.164	57
Products	**Revenue ($\$\,\mathrm{kg}^{-1}$)**	**Ref**
Oleic acid	1.40	58, 59
Glycerol	0.842	60, 61
Epoxidized fatty acid	2.805	62, 63
Glyceraldehyde	10243	64

Table S27 | Cost and revenues analysis for the simplified comparative techno-economic analysis of integrated domino photocatalytic valorization of fatty waste.

Category	**Inventory[1]**	**Quantity**	**Unity**	**Cost/Revenue ($)**
Input	Melamine	0.87	kg	1.39
	NaCl	8.66	kg	23.4
	Hydrochloric acid$_{(aq)}$ (37%)	6.05	kg	0.907
	Polypropylene[2]	3.52	kg	-0.130
	Liquid nitrogen	9.24	kg	8.13
	iCALB	2.23	kg	6983
	Ethyl acetate	65.1	kg	72.9
	Electricity[3]	88.5	kWh	14.5
Total relative cost ($)				7104
Output	Oleic acid	103	kg	144
	Glycerol	132	kg	111
	Epoxy fatty acids	1	kg	2.81
	Glyceraldehyde	1.52	kg	15569
Total relative revenue ($)				15827
Return on investment (ROI)				2.23

[1] Only inventory components that differ between the processes for domino valorization and for conventional biodiesel synthesis were included.

[2] Negative cost to account for a gate fee awarded for collecting municipal waste.[51]

[3] The electricity input for glycerol purification by distillation (~58 kWh) was included.[65, 66]

Table S28 | Economical hotspot analysis of integrated photocatalytic domino valorization of fatty waste.

Component	**Contribution (%)**
iCALB	98.3
Ethyl acetate	1.03
Sodium chloride	0.33
Energy	0.20
Liquid nitrogen	0.11
Hydrogen chloride$_{(aq)}$ (37%)	0.01

Table S29 | Sensitivity analysis of integrated photocatalytic domino photocatalytic valorization of fatty waste on relative costs, revenues and ROIs determined for the simplified comparative techno-economic analysis.

Parameter	**Pessimistic**			**Optimistic**		
	Relative costs ($)	Relative revenues ($)	ROI	Relative costs ($)	Relative revenues ($)	ROI
Photocatalyst (H-CN$_x$/PP) recyclability (1 cycle - 10 cycles -100 cycles)	7452	15827	2.12	7003	15827	2.26
iCALB recyclability (1 cycle - 10 cycles -100 cycles)	69947	15827	0.23	819	15827	19.3
Yield of epoxidized fatty acids (x0.5 - x1 - x5)	7104	15826	2.23	7104	15838	2.23
Yield of glyceraldehyde (x0.5 - x1 - x5)	7104	8042	1.13	7104	78105	11.0
Process ethyl acetate (29 L - 6.5 L - 1.2 L)	7357	15827	2.15	7045	15827	2.25

Supporting References

1. Z. Chen, A. Savateev, S. Pronkin, V. Papaefthimiou, C. Wolff, M. G. Willinger, E. Willinger, D. Neher, M. Antonietti and D. Dontsova, *Advanced Materials*, 2017, **29**, 1700555.
2. A. Rogolino, I. F. Silva, N. V. Tarakina, M. A. R. da Silva, G. F. S. R. Rocha, M. Antonietti and I. F. Teixeira, *ACS Applied Materials & Interfaces*, 2022, **14**, 49820-49829.
3. Y. Zhang, Q. Cao, A. Meng, X. Wu, Y. Xiao, C. Su and Q. Zhang, *Advanced Materials*, 2023, **35**, 2306831.
4. F. He, Y. Lu, Y. Wu, S. Wang, Y. Zhang, P. Dong, Y. Wang, C. Zhao, S. Wang, J. Zhang and S. Wang, *Advanced Materials*, 2023, **36**, 2307490.
5. L.-L. Liu, F. Chen, J.-H. Wu, J.-J. Chen and H.-Q. Yu, *Proceedings of the National Academy of Sciences*, 2023, **120**, e2215305120.
6. A. Rogolino, S. Linley, P. K. Kwarteng, S. A. Bonke, C. Pulignani, E. Reisner, *Chem*, 2026, *in print* (https://doi.org/10.1016/j.chempr.2025.102827)
7. S. Landi, I. R. Segundo, E. Freitas, M. Vasilevskiy, J. Carneiro and C. J. Tavares, *Solid State Communications*, 2022, **341**, 114573.
8. J. W. Kim and A. Kim, *Current Applied Physics*, 2021, **31**, 52-59.
9. J. W. Kim, A. Kim, H. U. Hwang, J. H. Kim, S. Choi, N. Koch, D. Shin, Z. Zhao, F. Liu, M. Choi, K. M. Lee and Y. Park, *Journal of Vacuum Science & Technology A*, 2023, **41**, 053211.
10. *Journal of Electroanalytical Chemistry and Interfacial Electrochemistry*, 1986, **209**, 417-428.
11. L. Jing, Z. Li, Z. Chen, R. Li and J. Hu, *Angewandte Chemie*, 2024, **136**, e202406398.
12. A. J. Bard, R. Parsons and J. Jordan, *Standard potentials in aqueous solution*, Routledge, 2017.
13. V. W.-h. Lau, I. Moudrakovski, T. Botari, S. Weinberger, M. B. Mesch, V. Duppel, J. Senker, V. Blum and B. V. Lotsch, *Nature Communications*, 2016, **7**, 12165.
14. E. M. Roth and E. S. Shanley, *Industrial & Engineering Chemistry*, 1953, **45**, 2343-2349.
15. W. D. Nicoll and A. F. Smith, *Industrial & Engineering Chemistry*, 1955, **47**, 2548-2554.
16. T. Cogliano, V. Russo, R. Turco, E. Santacesaria, M. Di Serio, T. Salmi and R. Tesser, *Chemical Engineering Science*, 2022, **251**, 117488.
17. F. P. Byrne, S. Jin, G. Paggiola, T. H. M. Petchey, J. H. Clark, T. J. Farmer, A. J. Hunt, C. Robert McElroy and J. Sherwood, *Sustainable Chemical Processes*, 2016, **4**, 7.
18. P. P. D. Minh, D.-V. Nguyen, M. C. Nguyen, N. H. Anh, H. P. Toan, P. P. Ly, N. L. Nguyen, T. Van Nguyen, M.-T. Pham, T. D. T. Ung, D. D. Bich, P. T. Hue, N. T. N. Hue, V.-H. Dang, W. J. Yu, S. H. Hur, Q. H. Nguyen, L. A. Tuyen and H.-T. Vuong, *Small Methods*, 2024, **9**, 2400797.
19. H. Ling, H. Sun, L. Lu, J. Zhang, L. Liao, J. Wang, X. Zhang, Y. Lan, R. Li, W. Lu, L. Cai, X. Bai and W. Wang, *Nature Communications*, 2024, **15**, 9505.
20. G. d. S. Martins, A. Staudt, F. K. Sutili, C. R. A. Malafaia and I. C. R. Leal, *Biotechnology Letters*, 2022, **44**, 867-878.
21. R. Battino, T. R. Rettich and T. Tominaga, *Journal of Physical and Chemical Reference Data*, 1983, **12**, 163-178.
22. T. H. G. Saji, J. M. Vicent-Luna, T. J. H. Vlugt, S. Calero and B. Bagheri, *Journal of Molecular Liquids*, 2024, **401**, 124530.
23. W. C. Schumb, C. N. Satterfield and R. L. Wentworth, *HYDROGEN PEROXIDE. PART 2. (CHAPTERS 5-6. REPORT NO. 43)*, United States, 1953.
24. G. D'Errico, O. Ortona, F. Capuano and V. Vitagliano, *Journal of Chemical & Engineering Data*, 2004, **49**, 1665-1670.
25. G. Papps and D. F. Othmer, *Industrial & Engineering Chemistry*, 1944, **36**, 430-434.
26. T. Särkkä, M. Gutiérrez-Poch and M. Kuhlberg, in *Technological Transformation in the Global Pulp and Paper Industry 1800–2018: Comparative Perspectives*, eds. T. Särkkä, M. Gutiérrez-Poch and M. Kuhlberg, Springer International Publishing, Cham, 2018, DOI: 10.1007/978-3-319-94962-8_1, pp. 1-10.
27. V. Aryan and A. Kraft, *Journal of Cleaner Production*, 2021, **280**, 124616.
28. E. A. Bried, Epoxidation of tall oil fatty acids and esters, *US3207743A*, United States, 1963.
29. FMC Corp, Epoxidation of fatty acids, *GB772151A*, United Kingdom, 1967.
30. K. Zoltán, *Journal of Chemical Research*, 2024, **48**, 17475198231226386.
31. J. Yang, C. Xu, B. Li, G. Ren and L. Wang, *Journal of Chemical Education*, 2013, **90**, 1362-1364.
32. S. Kim, C. Jiménez-González and B. E. Dale, *The International Journal of Life Cycle Assessment*, 2009, **14**, 392-400.
33. R. Frischknecht, N. Jungbluth, H.-J. Althaus, G. Doka, R. Dones, T. Heck, S. Hellweg, R. Hischier, T. Nemecek, G. Rebitzer and M. Spielmann, *The International Journal of Life Cycle Assessment*, 2005, **10**, 3-9.

34. T. Uekert, A. Singh, J. S. DesVeaux, T. Ghosh, A. Bhatt, G. Yadav, S. Afzal, J. Walzberg, K. M. Knauer, S. R. Nicholson, G. T. Beckham and A. C. Carpenter, *ACS Sustainable Chemistry & Engineering*, 2023, **11**, 965-978.
35. M. A. Tribe and R. L. W. Alpine, *Engineering Costs and Production Economics*, 1986, **10**, 271-278.
36. J. H. Walton and H. A. Lewis, *Journal of the American Chemical Society*, 1916, **38**, 633-638.
37. R. T. Ferrell and D. M. Himmelblau, *Journal of Chemical & Engineering Data*, 1967, **12**, 111-115.
38. A. Schumpe and P. Luehring, *Journal of Chemical & Engineering Data*, 1990, **35**, 24-25.
39. A. L. Imbault and R. Farnood, *Catalysts*, 2020, **10**.
40. E. L. Cussler, *Diffusion: mass transfer in fluid systems*, Cambridge university press, 2009.
41. V. R. Battula, G. Mark, M. S. Naeem, Y. Shah, M. Volokh, L. M. Gilbertson, N. López and M. Shalom, *Journal of the American Chemical Society*, 2025, **147**, 26739-26747.
42. E. Arkhangelsky, I. Levitsky and V. Gitis, *Water Supply*, 2017, **17**, 1212-1218.
43. P. Zhang, X. Chen, Y. Leng, Y. Dong, P. Jiang and M. Fan, *Fuel*, 2020, **272**, 117680.
44. C. Ortiz, M. L. Ferreira, O. Barbosa, J. C. S. dos Santos, R. C. Rodrigues, Á. Berenguer-Murcia, L. E. Briand and R. Fernandez-Lafuente, *Catalysis Science & Technology*, 2019, **9**, 2380-2420.
45. ChemAnalyst, *Hydrochloric acid Price Trend and Forecast, for the quarter ending June 2025*, accessible at: https://www.chemanalyst.com/Pricing-data/hydrochloric-acid-61 (Accessed: December 2025).
46. Imarc, *Hydrochloric Acid Prices, Trend, Chart, Demand, Market Analysis, News, Historical and Forecast Data Report 2025 Edition*, Report ID: SR112025A22323, accessible at: https://www.imarcgroup.com/hydrochloric-acid-pricing-report (Accessed: December 2025).
47. Imarc, *Melamine Prices, Trend, Chart, Demand, Market Analysis, News, Historical and Forecast Data Report 2025 Edition*, Report ID: SR112025A22318, accessible at: https://www.imarcgroup.com/melamine-pricing-report (Accessed: December 2025).
48. X. Yin, H. Liu, J. Webster, K. Trieu, M. D. Huffman, J. J. Miranda, M. Marklund, J. H. Y. Wu, L. K. Cobb, K. C. Li, S.-A. Pearson, B. Neal and M. Tian, *JMIR Public Health Surveill*, 2021, **7**, e27423.
49. Liquid Nitrogen Suppliers | Cryoniq. Available at: https://www.cryoniq.com/cryo-chamber-guide/before-ordering-equipment/liquid-nitrogen (Accessed: December 2025).
50. Liquid Nitrogen Pricing | Liquid Nitrogen Generators US LLC. Available at: https://liquidnitrogengeneratorsus.com/liquid-nitrogen-pricing/#:~:text=Liquid%20nitrogen%20(LN2)%20pricing%20in,per%20liter%20for%20bulk%20deliveries (Accessed: December 2025).
51. Dick, H. & Scholes, P. *Gate Fees 2017/18 Final Report: Comparing the Costs of Alternative Waste Treatment Options*. (WRAP, 2018).
52. Lipase acrylic resin | Sigma Aldrich. Available at: https://www.sigmaaldrich.com/GB/en/product/sigma/l4777 (Accessed: December 2025).
53. Lipase acrylic resin from Candida antarctica 5,000 U/g, recombinant, expressed in *Aspergillus niger* | Oakwood Chemical. Available at: https://www.oakwoodchemical.com/ProductsList.aspx?CategoryID=-2&txtSearch=162610&ExtHyperLink=1 (Accessed: December 2025).
54. Imarc, *Ethyl Acetate Prices, Trend, Chart, Demand, Market Analysis, News, Historical and Forecast Data Report 2025 Edition*, Report ID: SR112025A22380, accessible at: https://www.imarcgroup.com/ethyl-acetate-pricing-report (Accessed: December 2025).
55. Business Analytiq, Ethyl Acetate Price index, accessible at: https://businessanalytiq.com/procurementanalytics/index/ethyl-acetate-price-index/ (Accessed: December 2025).
56. ChemAnalyst, *Ethyl Acetate Price Trend and Forecast, for the quarter ending June 2025*, accessible at: https://www.chemanalyst.com/Pricing-data/ethyl-acetate-75 (Accessed: December 2025).
57. Eurostat, *Electricity price statistics*, accessible at: https://ec.europa.eu/eurostat/statistics-explained/index.php?title=Electricity_price_statistics (Accessed: December 2025).
58. ChemAnalyst, *Oleic Acid Price Trend and Forecast, for the quarter ending June 2025*, accessible at: https://www.chemanalyst.com/Pricing-data/oleic-acid-1284 (Accessed: December 2025).
59. Imarc, *Oleic Acid Prices, Trend, Chart, Demand, Market Analysis, News, Historical and Forecast Data Report 2024 Edition*, Report ID: SR112025A22368, accessible at: https://www.imarcgroup.com/oleic-acid-pricing-report (Accessed: December 2025).
60. Business Analytiq, Glycerol Price index, accessible at: https://businessanalytiq.com/procurementanalytics/index/glycerol-price-index/ (Accessed: December 2025).
61. Imarc, *Glycerin Prices, Trend, Chart, Demand, Market Analysis, News, Historical and Forecast Data Report 2025 Edition*, Report ID: SR112025A22478, accessible at: https://www.imarcgroup.com/glycerin-pricing-report (Accessed: December 2025).

62. Oleic Acid | Sigma-Aldrich. Available at: https://www.sigmaaldrich.com/GB/en/substance/oleicacid28246112801 (Accessed: December 2025).
63. Epoxidized Soybean Oil (ESO/ESBO)| alibaba.com. Available at: https://www.alibaba.com/product-detail/Epoxidized-Soybean-Oil-ESO-ESBO-CAS_1600546177783.html (Accessed: December 2025).
64. DL-Glyceraldehyde | Sigma-Aldrich. Available at: https://www.sigmaaldrich.com/GB/en/product/sigma/g5001 (Accessed: December 2025).
65. K. Yong, T. Ooi, K. Dzulkefly, W. Wan Yunus and A. Hazimah, *Journal of Oil Palm Research*, 2001, **13**, 39-44.
66. A. Hazimah, T. Ooi and A. Salmiah, *Journal of Oil Palm Research*, 2003, **16**, 1-5.